










RESEARCH ARTICLE | MARCH 07 2022

Dependence of the L–H power threshold on the alignment of external non-axisymmetric magnetic perturbations in ASDEX Upgrade

M. Willensdorfer ; U. Plank; D. Brida ; M. Cavedon ; G. D. Conway; D. A. Ryan; W. Suttrop ; R. Buchholz; M. Dunne; R. Fischer; M. Griener ; J. Hobirk ; S. Kasilov; A. Kirk ; R. M. McDermott ; T. Pütterich; G. Tardini; Q. Yu ; ASDEX Upgrade Team.; MST1 Team



Phys. Plasmas 29, 032506 (2022)

<https://doi.org/10.1063/5.0073841>



AIP Advances

Why Publish With Us?

	25 DAYS average time to 1st decision		740+ DOWNLOADS average per article		INCLUSIVE scope
---	---	---	--	---	---------------------------

[Learn More](#)



Dependence of the L–H power threshold on the alignment of external non-axisymmetric magnetic perturbations in ASDEX Upgrade

Cite as: Phys. Plasmas **29**, 032506 (2022); doi: [10.1063/5.0073841](https://doi.org/10.1063/5.0073841)

Submitted: 4 October 2021 · Accepted: 10 February 2022 ·

Published Online: 7 March 2022



View Online



Export Citation



CrossMark

M. Willensdorfer,^{1,a)} U. Plank,¹ D. Brida,¹ M. Cavedon,² G. D. Conway,¹ D. A. Ryan,³ W. Suttrop,¹ R. Buchholz,⁴ M. Dunne,¹ R. Fischer,¹ M. Griener,¹ J. Hobirk,¹ S. Kasilov,⁴ A. Kirk,³ R. M. McDermott,¹ T. Pütterich,¹ G. Tardini,¹ Q. Yu,¹ ASDEX Upgrade Team,⁵ and MSTI Team⁶

AFFILIATIONS

¹Max Planck Institute for Plasma Physics, 85748 Garching, Germany

²Dipartimento di Fisica “G. Occhialini,” Università di Milano-Bicocca, 20126 Milano, Italy

³CCFE, Culham Science Centre, Abingdon OX14 3DB, United Kingdom

⁴Fusion@ÖAW, Institut für Theoretische Physik-Computational Physics, TU Graz, 8010 Graz, Austria

⁵See author list of H. Meyer *et al.*, Nucl. Fusion **59**, 112014 (2019).

⁶See author list of B. Labit *et al.*, Nucl. Fusion **59**, 102014 (2019).

^{a)} Author to whom correspondence should be addressed: matthias.willensdorfer@ipp.mpg.de

ABSTRACT

Experiments at ASDEX Upgrade have been conducted to study the impact of the alignment of external magnetic perturbations (MPs) with $n = 2$ toroidal mode symmetry on the power threshold of the transition from L- to H-mode (P_{LH}). This is interesting for ITER, since its operation will rely on a MP field configuration that securely suppresses edge localized modes (ELMs) while avoiding an increase in the L–H power threshold. P_{LH} can increase up to $\approx 80\%$ when the external MP field is aligned to maximize the associated plasma response at the edge. This alignment deviates from the equilibrium field pitch and is similar to the one that is required to suppress ELMs by MPs in H-mode. The relative radial magnetic field perturbation $\delta B_r/B_T$ has to exceed a critical value, roughly $1.7 - 2 \times 10^{-4}$ (at the $q = 5$ surface), to cause an increase in P_{LH} . This value is above the one that is required to sustain ELM suppression at ASDEX Upgrade. Combining plasma response calculations with a critical value of $\delta B_r/B_T$ captures well the measured dependencies of P_{LH} on the alignment of the applied MP field. The increase in P_{LH} is accompanied by a change in the $\mathbf{E} \times \mathbf{B}$ flow velocity ($v_{E \times B}$) profile. The application of MPs in L-mode flattens and reverses the edge $v_{E \times B}$ profile when at least $\delta B_r/B_T \approx 1.9 \times 10^{-4}$ is applied. This is the same value above which P_{LH} increases. More heating power is needed to roughly achieve the same shear in the $v_{E \times B}$ profile at the transition to H-mode as without MPs but with an $v_{E \times B}$ profile that is shifted into the ion diamagnetic direction.

© 2022 Author(s). All article content, except where otherwise noted, is licensed under a Creative Commons Attribution (CC BY) license (<http://creativecommons.org/licenses/by/4.0/>). <https://doi.org/10.1063/5.0073841>

I. INTRODUCTION

The power loss from a single edge localized mode (ELM) in high confinement mode (H-mode) plasmas could already be devastating for future fusion devices such as ITER.¹ To reduce the power loss from ELMs, including the first one, ITER may apply non-axisymmetric magnetic perturbations (MPs) in a low confinement mode (L-mode) prior to the transition to H-mode.² Since the auxiliary heating power of ITER will be marginally above the power threshold needed to enable the transition from L-mode to H-mode (L–H transition), it is important to

understand the impact of externally applied non-axisymmetric MPs and, thus, error fields on the L–H power threshold (P_{LH}). The study of the interaction between error fields and P_{LH} ³ may also shed some light on differences between various machines in multi-machine databases⁴ since every machine has a different intrinsic error field.

Several studies suggest that a sufficiently large shearing rate of the $\mathbf{E} \times \mathbf{B}$ flow velocity ($v_{E \times B}$) at the edge is required to suppress turbulence^{5,6} and, thus, establish an edge transport barrier leading to H-mode. The required radial electric field (E_r) profile is, according to

neoclassical theory, mainly determined by the main ion pressure gradient at the edge via the diamagnetic velocity. This pressure gradient is partially set by the ion temperature (T_i) profile, which is actuated by the auxiliary heating power.⁷ Recent measurements at different toroidal magnetic fields (B_{T^S}) further identify the role of a critical minimum in the $v_{E \times B}$ profile⁸ rather than in the E_r profile.⁹ The criterion of a critical $v_{E \times B}$ minimum is only an approximation for the shear between the minimum of the $v_{E \times B}$ profile and the inner or outer part of the $v_{E \times B}$ profile assuming those are not changing. The criterion of a critical shear in $v_{E \times B}$ allows one to reproduce main dependences in P_{LH} from a multi-machine database⁴ such as B_T , electron density (n_e), and surface S .^{8,10}

Previous studies at MAST^{11,12} and DIII-D^{13,14} suggest that the application of an external MP-field induces an ergodic layer in the L-mode, which reverses and flattens the E_r profile at the edge. This hampers the access to the H-mode and increases significantly P_{LH} in MAST [by up to 100% (Ref. 12)], DIII-D,^{13–15} KSTAR,^{16,17} and NSTX.¹⁸ It has also been proposed that additional turbulent transport due to the external MP-field flattens the edge pressure gradient primarily due to changes in the density profile.¹⁴ Studies at ASDEX Upgrade (AUG)^{19,20} suggested that the MP field flattens the edge pressure gradient primarily due to a flattened temperature profile. Consequently, more heating power is necessary to achieve the same gradients in edge pressure profiles and, thus, the same shearing rate of the $v_{E \times B}$ profile. Unlike the results from DIII-D,^{13–15} MAST,^{11,12} and KSTAR,^{16,17} studies at AUG^{19,20} showed almost no increase in P_{LH} at densities around the minimum of P_{LH} and only a moderate increase by 20% for higher densities. Although a reversal in the edge E_r in the L-mode has been observed in AUG,²¹ a correlation to the increase in P_{LH} has not been measured.²⁰

In this paper, we extend previous studies in AUG^{19,20} toward larger relative MP field strength using a toroidal mode symmetry n of 2. This is possible by using the full set of 16 MP coils instead of the initial setup of 8 as in 2011. Additionally, we operate at B_T of 1.8 T (instead of 2.5 T), which increases the relative MP field perturbation $\delta B/B_T$ and allows us to raise the tolerable applied current of a single coil from 1 to 1.3 kA. In total, the relative MP field strength increases by a factor of up to ≈ 2.6 with respect to previous studies.¹⁹ We also study the impact of the applied poloidal mode spectrum on the L–H power threshold using the alignment of the MP field with respect to the equilibrium field pitch. This is particularly important for ITER since the phasing is essential for ELM suppression^{22,23} and might lead to a possibility to minimize the increase in L–H power threshold while maximizing the probability to access ELM suppression. Additional experiments are conducted to probe possible error field effects and toroidal asymmetries on edge kinetic and $v_{E \times B}$ profiles before L–H transition by varying the absolute phase of the MP field while keeping the applied poloidal mode spectrum constant. These experiments allow us to connect previously observed changes in the edge $E_r/v_{E \times B}$ profile²¹ with the increase in P_{LH} .²⁰

This paper is arranged as follows: In Sec. II, the experimental setup is briefly described. The impact of the applied poloidal mode spectrum on the L–H power threshold and comparison with the plasma response model are shown in Sec. III. Section IV shows changes in the $v_{E \times B}$ profiles and discusses possible toroidal asymmetries. In Sec. V, various models are compared to the experimental finding. Summary and conclusions are given in Sec. VI.

II. EXPERIMENTAL SETUP

Before we report on experimental results, the setup of the external MP coils, essential diagnostics, and the discharge configuration is briefly introduced.

A. MP-coil and diagnostic setup

AUG has two rows of external MP coils with eight coils in each row above and below the midplane. The coil setup is suitable to produce external MP-fields using toroidal mode symmetries of $n = 1, 2, 3$, and 4. In this paper, we focus on the application of an $n = 2$ MP field, which is also used for ELM suppression. The applied poloidal mode spectrum depends on the relative alignment between the field lines and the MP field. Thus, it depends on the safety factor (q) profile and the differential phase angle ($\Delta\varphi_{UL}$) between the MP field from the upper and lower coil set. All 16 coils are supplied by 16 independent power supplies,²⁴ which allows us to program different $\Delta\varphi_{UL}$ s with an arbitrary orientation of the MP field set by the absolute toroidal phase angle (ϕ_0). This enables us to study possible toroidal asymmetries induced by the applied three-dimensional (3D) MP-field. The MP coils are mounted close to a passive stabilization loop (PSL), which is a copper conductor. The resulting eddy currents delay and attenuate the MP field at the plasma surface. This is taken into account by an effective coil current based on finite elements method calculations.²⁵

To investigate L–H transitions in the presence of an external MP field, electron and ion temperature and density profiles are essential. The electron temperature profiles are measured by the electron cyclotron emission (ECE),^{26,27} the helium beam (HEB),²⁸ and the Thomson scattering (TS) diagnostics. To evaluate measurements from TS, the integrated data analysis (IDA)²⁹ is used. TS and HEB are able to determine the edge electron density profile as well. The line integrated density is measured by an interferometer using a deuterium cyanide (DCN) laser.³⁰ An X-mode Doppler reflectometry (DR),²¹ charge exchange recombination spectroscopy (CXRS)^{31,32} using nitrogen N^{7+} , and a new active He⁺ spectroscopy (HES) measure the radial electric field E_r and, thus, $v_{E \times B} = E_r/B$ before the L–H transition. The HES³³ diagnostic is based on injected thermal helium, which is ionized and excited by electron impact. Similar to CXRS, it is based on measuring all components of the local radial electric field E_r profile via the radial force balance defined for arbitrary ion species α by

$$E_r^\alpha = \left(\frac{\nabla P_i}{n_i Z} \right)^\alpha - v_{\text{pol}}^\alpha B_{\text{tor}} + v_{\text{tor}}^\alpha B_{\text{pol}}. \quad (1)$$

The poloidal velocity v_{pol}^α for He¹⁺ (and N⁷⁺) is usually the dominant term, whereas the toroidal velocity v_{tor}^α term is small due to the large toroidal magnetic field B_{tor} (≈ 1.4 T) and the small poloidal magnetic field B_{pol} (≈ 0.3 T) at the measurement position around the outer midplane. The diamagnetic term for He¹⁺ is also small, since the relevant temperatures and densities are those of the injected helium. For background subtraction, the injected thermal helium beam is chopped (10 or 20 ms on and off are used). The big advantage of the HES diagnostic is that it is able to deliver E_r profiles with high temporal resolution (3 ms) without the need of information from another diagnostics (such as n_e in DR) or a neutral beam injection (NBI) source. In comparison, for example, the single channel DR at AUG takes 110 ms (in the chosen configuration) for one sweep (one E_r profiles) to achieve a good

coverage with excellent spatial resolution at the plasma edge. Details about these diagnostics can be found in the corresponding references.

B. Discharge configuration

The discharge configuration has been adapted from previous L–H transition studies,⁸ and typical plasma parameters do not deviate more than 15% from the scenario used to study ELM suppression.²³ Typical parameters of the deuterium plasmas are B_T of 1.83 T with the grad B drift direction to the divertor (favorable direction for H-mode access), a plasma current (I_p) of 0.8 MA, and a safety factor at the edge (q_{95}) of 3.8. The line integrated core density \bar{n}_e has been feedback controlled to $3.5 \times 10^{19} \text{ m}^{-2}$, which is close to the density, according to Eq. (3) in Ref. 7, where the minimum of P_{LH} is expected ($n_{e,min}^{scal} \approx 3.3 \times 10^{19} \text{ m}^{-3}$). This makes P_{LH} and, therefore, our analysis less sensitive to variations in the plasma density. In a few experiments, we injected a small amount of nitrogen ($0.5 - 1 \times 10^{20} \text{ s}^{-1}$) to enhance CXRS measurements. As we will see later, this amount of nitrogen does not influence P_{LH} .

The experiments are designed to induce several L–H transitions during the flat top phase of the plasma current [Fig. 1(a)]. Each L–H transition is induced by slowly ramping up the NBI power (P_{NBI}) using reduced voltage beams (1.6–2 MW/source) and varying the duty cycle. This results in a slow increase in the net heating power (P_{NET}) [Fig. 1(a)] given by $P_{NET} = P_{OH} + P_{NBI} - dW_{MHD}/dt$, where W_{MHD} is the plasma energy and P_{OH} is the Ohmic heating power. The very first NBI phase [Fig. 1(a)] was applied to extend the available Ohmic heating flux, thereby sustaining the flattop phase of I_p . This very first NBI phase is excluded from the analysis. In between the three subsequent NBI phases, we varied the applied poloidal mode spectrum via $\Delta\varphi_{UL}$ and/or the orientation of the absolute phase ϕ_0 of the MP field. The MP field strength was kept the same. In the presented example (Fig. 1), we used $\Delta\varphi_{UL} \approx 135^\circ$ and switched ϕ_0 from 135° to 225° .

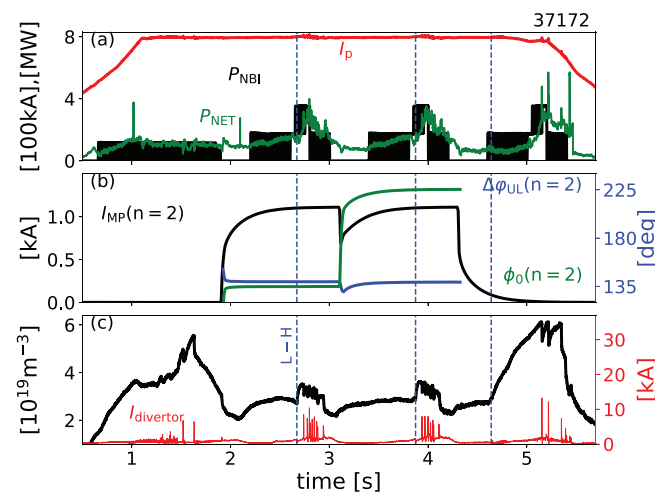


FIG. 1. Time traces from (a) the plasma current, NBI power (P_{NBI}), and net heating power (P_{NET}), (b) $n = 2$ MP field amplitude in kA (black), differential phase angle $\Delta\varphi_{UL}$ (blue), absolute orientation ϕ_0 (green), (c) line averaged density (black) and divertor current (red). Timing of three L–H transitions is indicated by blue vertical dashed lines. The applied MP field clearly postpones L–H transitions with respect to the onset of the NBI ramp.

During the last NBI ramp, the MP field was turned off. Because of the delay from the aforementioned eddy currents, the MP field is not exactly zero at the onset of the last NBI ramp.

To identify the L–H transition, we use the thermoelectric current in the divertor and the onset of the accompanied increase in density [Fig. 1(c) and later in Fig. 8]. If the plasma dithers between the L-mode and H-mode, then the beginning of the dithering phase is used as the onset of L–H transition. To determine P_{LH} , P_{NET} is averaged within a time window of 10 ms around the maximum of P_{NET} close to L–H transition. The radiated power is not taken into account as was done in the power threshold scaling ($P_{LH,08}$) from the multi-machine database in Ref. 4.

C. Dataset

We collected data over three campaigns between the years 2017 and 2020. In total, we conducted 15 discharges including 34 useful L–H transitions with and without the $n = 2$ MP-field. L–H transitions with obvious $n = 1$ locked modes (LMs) are excluded. During the 2018/2019 campaign, one coil of the lower set (B15) was accidentally incorrectly wired, which had been noticed after the campaign. The result is an incorrectly set polarity of one coil, which unintentionally introduced an $n = 1$ MP field and reduces the amplitude of the $n = 2$ MP field. An important quantity is the relative radial field perturbation of the resonant component ($\delta B_{r,res}/B_T$) from the external MP field integrated along the closed magnetic lines on a rational magnetic surface.¹⁵ Figure 2 shows $\delta B_{r,res}/B_T$ from $n = 1$ and $n = 2$ at the $q = 5$ surface vs the $n = 2$ amplitude of the applied MP coil current ($I_{n=2}$). The wrongly polarized coil current reduces $I_{n=2}$ by up to 20%. The additional $n = 1$ component $\delta B_{r,res}^{n=1}/B_T$ varies between $0 - 1 \times 10^{-4}$. The predicted $n = 1$ component is small and has a similar magnitude as the intrinsic $n = 1$ error field of AUG, which ranges from $0.2 - 0.5 \times 10^{-4}$ at B_T of 1.5 T.³⁴

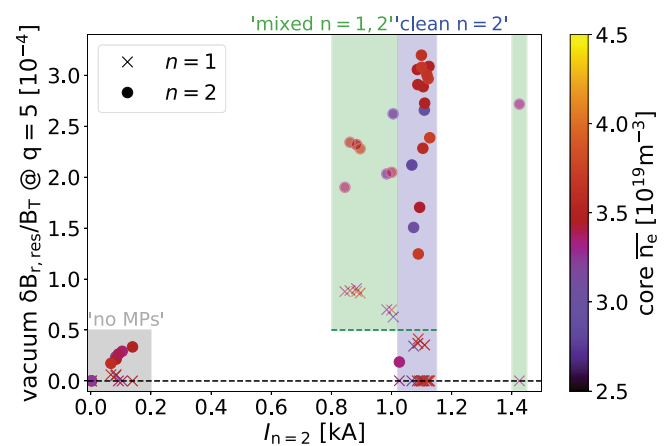


FIG. 2. Dataset includes 34 L–H transitions with and without the dominant $n = 2$ MP field. Applied relative MPs of the resonant component ($\delta B_{r,res}/B_T$) from $n = 1$ (crosses) and $n = 2$ (circles) at the $q = 5$ surface vs the $n = 2$ amplitude (in kA) of the MP-coil current averaged over both rows. Each point in the dataset is represented by one cross and one circle at the same abscissa value. Color scaling indicates the range of densities. The shaded areas show the classification in L–H transitions with no MPs (gray), mixed $n = 1, 2$ (green, see text), and clean $n = 2$ (blue) used in this paper.

Since the cases from 2018/2019 may contain valuable information and to ensure no compromise from the $n = 1$ component on our analysis, we introduce the following classification:

- (i) data points with $I_{n=2} \approx 1 - 1.2$ kA and small $n = 1$ amplitude $\delta B_{r,\text{res}}^{n=1}/B_T < 0.5 \times 10^{-4}$ are labeled as “clean $n = 2$ ” (blue area in Fig. 2).
- (ii) data points with $I_{n=2} < 1$ kA and $\delta B_{r,\text{res}}^{n=1}/B_T > 0.5 \times 10^{-4}$ are labeled as “mixed $n = 1, 2$ ” (green area in Fig. 2). To this class, we add one data point with $I_{n=2} > 1.2$ kA due to larger $n = 2$ amplitude although no $n = 1$ MP-field was accidentally applied.
- (iii) $I_{n=2} < 0.2$ kA and $\delta B_{r,\text{res}}^{n=2}/B_T < 0.5 \times 10^{-4}$ are no MPs references (gray area in Fig. 2).

The presented classification is visualized by the colored shaded areas in Fig. 2. The range of the achieved line averaged core densities is illustrated by the color scaling of the symbols in Fig. 2. The density varies from 3.05 to $3.74 \times 10^{19} \text{ m}^{-3}$, and the mean value is $3.46 \pm 0.18 \times 10^{19} \text{ m}^{-3}$. The corresponding Greenwald fraction is $n_e/n_G \approx 0.3$. Since these values are around the expected minimum in P_{LH} ($n_{e,\text{min}}^{\text{scal}} \approx 3.3 \times 10^{19} \text{ m}^{-3}$, Ref. 7) we assume minimal impact of a density variation on the analysis.

III. CHANGE OF L-H POWER THRESHOLD

A. Dependence on the alignment from the MP-field

To study the influence of the alignment from the MP field on P_{LH} , Fig. 3 shows P_{LH} vs $\Delta\phi_{\text{UL}}$ using all L–H transitions in the dataset. As described previously, we distinguish between “clean $n = 2$ ” and “mixed $n = 1, 2$ ” marked as filled and transparent symbols, respectively. The range of P_{LH} without MPs are added as a horizontal gray bar, which is slightly below the predictions from the Martin scaling⁴ multiplied by the typical correction factor of 0.75 for AUG with the tungsten wall. The correction factor for P_{LH} at AUG is necessary since transition from the graphite wall to the full tungsten wall²⁰ an effect,

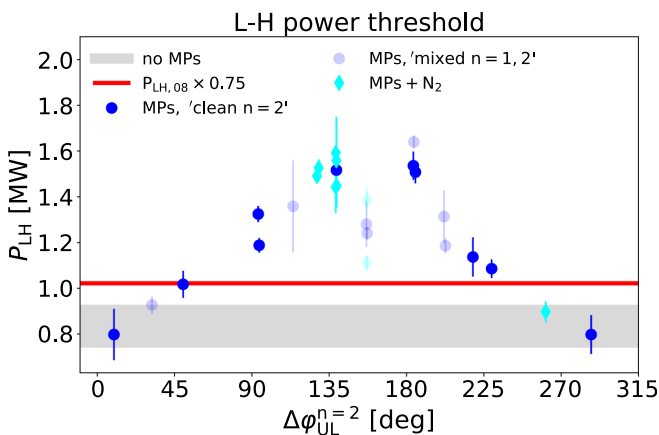


FIG. 3. P_{LH} vs applied differential phase angle $\Delta\phi_{\text{UL}}$ using $n = 2$. Reference measurements without MPs are within the horizontal gray bar. The horizontal red line is the L–H transition power threshold from the Martin scaling with a correction factor of 0.75 (Ref. 20). Discharges with a small amount of nitrogen for diagnostics are indicated by cyan symbols. The power threshold of L–H transition can increase by up to 80% with respect to no MPs references when $\Delta\phi_{\text{UL}}$ of 90° – 180° is applied.

which has also been observed at JET.³⁵ It is attributed to changes in the edge density profile caused by different behaviors of wall reflection of neutrals.³⁶ In some discharges, we added a small amount of N_2 to enhance CXRS measurements. This did not corrupt P_{LH} .

In our experiments, the application of MPs (considering clean $n = 2$ only) increases P_{LH} from $P_{\text{LH}}^{\text{noMPs}} = 0.83 \pm 0.09$ MW to $P_{\text{LH}}^{\text{wiMPs}} = 1.54 \pm 0.09$ MW by up to roughly 80%. The strongest increase in P_{LH} is observed around $\Delta\phi_{\text{UL}} \approx 135^\circ - 180^\circ$. Figure 3 further shows that the incorrect polarity of the single MP coil can have a significant effect, since the P_{LH} values around $\Delta\phi_{\text{UL}} \approx 150^\circ$ from the mixed $n = 1, 2$ dataset are clearly below the one from the neighboring clean $n = 2$ data points. As we will see in Sec. III C, this drop is caused by the reduced $n = 2$ amplitude.

B. Comparison to plasma response calculations

Since there are enough L–H transitions with a clean $n = 2$ spectrum in the dataset, we further study the $\Delta\phi_{\text{UL}}$ dependence of P_{LH} . We use linear resistive single fluid magnetohydrodynamic (MHD) calculations from MARS-F to predict the plasma response to the applied MP field. Details of the implementation of AUG equilibria in MARS-F can be found in Refs. 37 and 38. The presented MARS-F and VMEC calculations are based on an equilibrium from discharge 35712 at 2.65 s before the L–H transition. Figure 4(a) shows $\delta B_{r,\text{res}}$ of the rational surfaces at the edge using the vacuum approximation (dashed) and linear resistive MHD from MARS-F (solid). Figure 4(b) shows the resonant component of the dimensionless radial field perturbation³⁸ defined as $b_{\text{res}}^1 = \frac{q}{R_0^2 B_0} \frac{\mathbf{b} \cdot \nabla \Psi}{\mathbf{b}_{\text{eq}} \cdot \nabla \phi}$, where \mathbf{b}_{eq} is the equilibrium field, \mathbf{b} is the

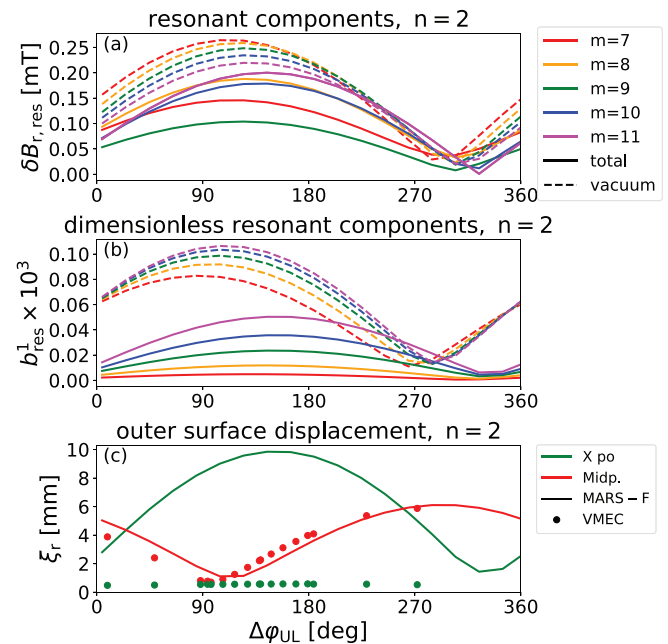


FIG. 4. Total (solid) and vacuum field perturbations (dashed) of $n = 2$ rational surfaces vs $\Delta\phi_{\text{UL}}$ using (a) resonant radial field components $\delta B_{r,\text{res}}$ and (b) dimensionless radial field perturbations b_{res}^1 from MARS-F as defined in the text. (c) Comparison of radial displacements (ξ_r) vs $\Delta\phi_{\text{UL}}$ between VMEC and MARS-F based on the equilibrium from discharge 35712 at 2.65 s.

perturbed field, R is the major radius, ϕ is the toroidal flux, Ψ is the poloidal flux, and B_0 is the magnetic field at the magnetic axis. We show $\delta B_{r,\text{res}}$ (later $\delta B_{r,\text{res}}/B_T$) and b_{res}^1 , because $\delta B_{r,\text{res}}/B_T$ has been used in previous L–H transition studies,^{14,15} whereas b_{res}^1 is used to predict best ELM mitigation and suppression.³⁸ Similar to H-mode cases,³⁸ there is a clear shift of around 40° in the maximum between b_{res}^1 calculated including the plasma response $\Delta\varphi_{\text{UL}} \approx 150^\circ$ and using only the vacuum field perturbations $\Delta\varphi_{\text{UL}} \approx 110^\circ$.

This observable shift of $\Delta\varphi_{\text{UL}}$ at the maximum P_{LH} away from the field alignment (maximum vacuum field perturbations) indicates the role of stable ideal kink modes, which has been extensively verified in H-mode experiments.^{22,39–41} However, in contrast to the H-mode, the plasma response in the L-mode reduces the resonant components by a factor of 2 due to plasma screening and missing amplification because of the flat pressure profile before the L–H transition.

The associated radial displacements of the plasma surface from MARS-F are illustrated in Fig. 4(c) and are compared to the results from the ideal MHD equilibrium code VMEC (see Ref. 26 for details of the implementation). Both codes agree well at the outer midplane [Fig. 4(c)] and have been tested against dedicated measurements at the outer midplane in H-mode.⁴¹ Since the minima of the radial displacement at the outer midplane are close to $\Delta\varphi_{\text{UL}}$, which maximizes P_{LH} , we do not expect to see large radial distortions in the profile measurements in these cases. MARS-F and VMEC do not agree at the X-point. This is attributed to different approaches, since VMEC is a non-linear ideal MHD code with nested flux surfaces constraining the displacement close to the X-point, whereas MARS-F is a linear resistive MHD code.⁴² Further comparison between VMEC and MARS-F is beyond the scope of this paper.

To compare directly the results from the MHD modeling with the variation in the L–H power threshold, Fig. 5 shows P_{LH} vs $\Delta\varphi_{\text{UL}}$ together with normalized $\widehat{b}_{\text{res}}^1 = b_{\text{res}}^1/\max(b_{\text{res}}^1)$ from MARS-F (solid lines) and from the vacuum solution (dashed). The colors indicate different rational surfaces for $n = 2$, and the associated poloidal mode numbers are added. The strongest correlation is seen between P_{LH} and

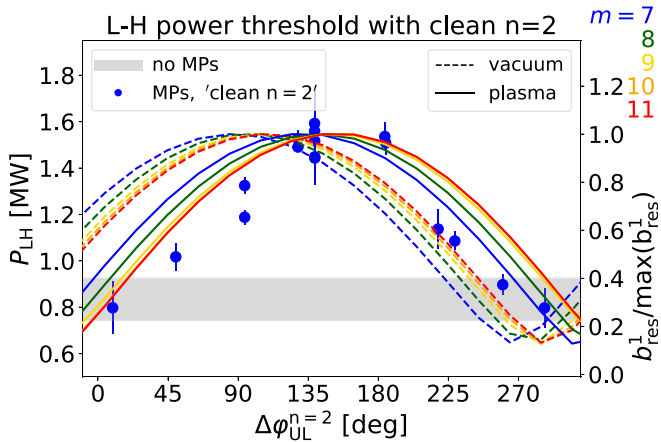


FIG. 5. L–H power threshold vs $\Delta\varphi_{\text{UL}}$ using clean $n = 2$ cases from Fig. 3 combined with resonant components of b_{res}^1 at $n = 2$ rational surfaces from Fig. 4(b) including plasma response (MARS-F, solid) and without it (vacuum, dashed). The maximum power threshold correlates with maximum b_{res}^1 from MARS-F at the edge (9/2, 10/2, 11/2).

the $\widehat{b}_{\text{res}}^1$ from MARS-F at the rational surfaces of 9/2, 10/2, and 11/2. These are three outermost $n = 2$ rational surfaces of the truncated equilibrium. Interestingly, the data-points around the flanks ($\Delta\varphi_{\text{UL}} \approx 225^\circ, 45^\circ - 90^\circ$) are below the $\widehat{b}_{\text{res}}^1$ curves (orange, red in Fig. 5) from the outermost surfaces. The reason for this will be resolved in Sec. III C.

C. Critical magnetic perturbation field strength

In Sec. III B, we have shown that the maximum in P_{LH} correlates with the maximum in radial field perturbation including the plasma response from MARS-F ($\delta B_{r,\text{res}}^{\text{pl}}$) from Fig. 4(a). Both deviate from the equilibrium field pitch indicating that the coupling between stable kink modes and resonant components at the edge play a role in L–H transition. The poloidal mode numbers that are a bit higher than the resonant components, i.e., $nq + 1$ and $nq + 2$, are the most important for the excitation of external kink modes.⁴³ To investigate their impact on P_{LH} , the $m = nq, nq + 1$, and $nq + 2$ poloidal mode components of the applied relative vacuum perturbations $\delta B_r/B_T$ (at the $q = 5$ surface) for each L–H transition in the database are related to P_{LH} in Fig. 6. To calculate the poloidal mode components, an equilibrium from

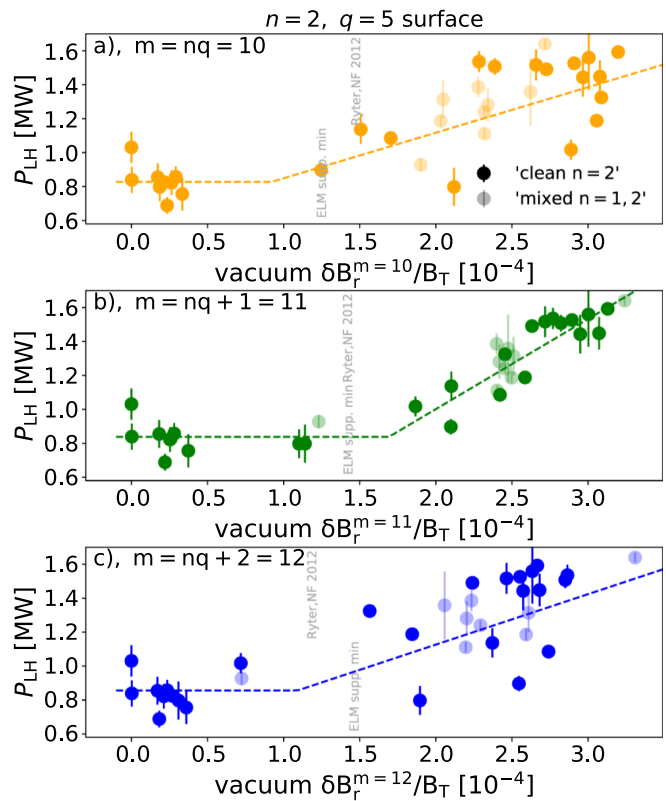


FIG. 6. L–H power threshold P_{LH} vs applied relative vacuum perturbations $\delta B_r/B_T$ of (a) resonant component $m = nq$, (b) $m = nq + 1$, and (c) $m = nq + 2$ poloidal components. Dashed lines are simple linear least squares fits to guide the eye. The gray text indicates values from previous AUG studies¹⁹ and values to sustain ELM suppression for several seconds (discharge 37 065). The $m = nq + 1$ component correlates best with P_{LH} , and a critical value of $\delta B_r/B_T \approx 1.7 - 2 \times 10^{-4}$ is needed to increase P_{LH} .

the CLISTE code⁴⁴ has been used for each datapoint. The best correlation is seen between the $nq + 1$ component and P_{LH} , which further supports the idea that the excitation of kink modes is essential. Moreover, a clear threshold effect is observed. A critical value ($\delta B_r^{\text{res}}/B_T \approx 1.7 - 2 \times 10^{-4}$) is needed to cause a rise in P_{LH} . Above this critical value, P_{LH} increases linearly with the perturbation magnitude, whereas below this value, no effect is seen. This behavior is also observed in resonant $m = nq$ and $nq + 2$ components, but much less pronounced. Analyzing $\delta B_r^m/B_T$ at a neighboring rational surface like $q = 9/2$ or $11/2$ leads to the same conclusion. A critical MP field strength needed to increase P_{LH} has also been observed in DIII-D,^{14,15} KSTAR,^{16,17} and MAST.¹² The vertical gray text “ELM suppr. Min” in Fig. 6 shows the minimum $\delta B_r/B_T$ values to sustain ELM suppression at AUG for several seconds (discharge 37065), which is below the critical value to increase P_{LH} . This indicates the possibility to sustain ELM suppression without increasing P_{LH} . Figure 6(b) also exemplifies why the reduction in the $n = 2$ amplitude rather than the additional $n = 1$ component in the mixed $n = 1, 2$ dataset is important. A reduction by $\sim 20\%$ in the $n = 2$ amplitude already lowers the P_{LH} by 0.3 MW, which halves the maximum increase due to the MPs.

The existence of a critical value of $\delta B_r^{\text{res}}/B_T$ for P_{LH} also explains why the $\Delta\varphi_{\text{UL}}$ dependence of P_{LH} does not exactly follow the trend from $B_{r,\text{res}}^{\text{pl}}$. To describe the behavior of P_{LH} correctly, we define an empirical critical function $f_{\text{LH}}^{\text{crit}}$ using the normalized radial field perturbation $\widehat{B}_{r,\text{res}}^{\text{pl}} = \delta B_{r,\text{res}}^{\text{pl}}/\max(\delta B_{r,\text{res}}^{\text{pl}})$,

$$f_{\text{LH}}^{\text{crit}}(\widehat{B}_{r,\text{res}}^{\text{pl}}) = P_{\text{LH}}^{\text{noMPs}} + \begin{cases} 0, & \widehat{B}_{r,\text{res}}^{\text{pl}} < 2/3 \\ (P_{\text{LH,max}}^{\text{wiMPs}} - P_{\text{LH}}^{\text{noMPs}}) \left(3\widehat{B}_{r,\text{res}}^{\text{pl}} - 2 \right), & \widehat{B}_{r,\text{res}}^{\text{pl}} \geq 2/3. \end{cases} \quad (2)$$

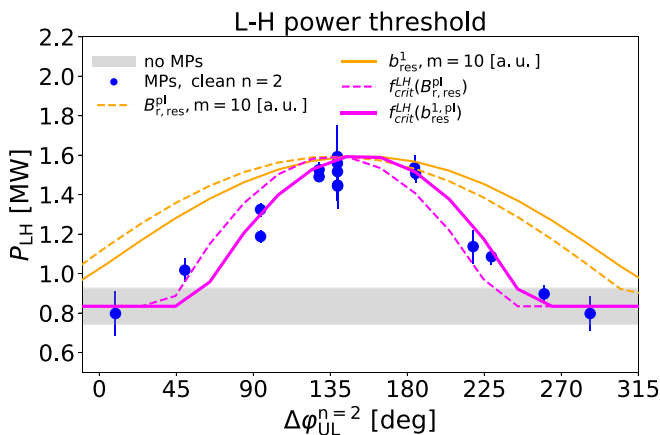


FIG. 7. L–H transition power threshold vs $\Delta\varphi_{\text{UL}}$. P_{LH} values from clean $n = 2$ (blue circles) are compared to b_{res}^1 (orange solid) and $B_{r,\text{res}}^{\text{pl}}$ (orange dashed) from MARS-F at the 10/2 surface and both combined with a critical function $f_{\text{LH}}^{\text{crit}}$ (magenta). Good agreement with measurements is found if a critical value for b_{res}^1 to increase P_{LH} is considered.

Below the critical value, $f_{\text{LH}}^{\text{crit}}$ is equal to the mean value of the no MPs cases. Above the critical value, a linear function is used such that $f_{\text{LH}}^{\text{crit}}$ is $P_{\text{LH,max}}^{\text{wiMPs}}$, when $\widehat{B}_{r,\text{res}}^{\text{pl}}$ reaches 1. We use 2/3 as a critical value of the maximum perturbation, because this is roughly observed in Fig. 6(b). The significant improvement by considering a critical value is demonstrated in Fig. 7. $f_{\text{LH}}^{\text{crit}}$ captures very well the $\Delta\varphi_{\text{UL}}$ behavior of the P_{LH} measurements, whereas the linear plasma response from (MARS-F) ($B_{r,\text{res}}^{\text{pl}}$) by itself does not. The same procedure has been applied using $\widehat{b}_{\text{res}}^1$ as parameter for $f_{\text{LH}}^{\text{crit}}$, which yields even better agreement with experiments.

The observation of a critical value is well in line with the results from other machines.^{14,15,45} Moreover, it explains the absence of a strong increase in P_{LH} due to MPs in previous AUG studies. At that time and the chosen configuration, the MP field was simply not strong enough to significantly increase P_{LH} (variations in other parameters like density might also play a role).

IV. E × B VELOCITY PROFILES

To further investigate the underlying mechanism behind the changes in P_{LH} , good knowledge of the kinetic and flow profiles, especially of the $v_{E \times B}$ profiles⁸ at the edge, is essential. An additional difficulty is that the applied MP field breaks the axisymmetry, and the edge profiles are not necessarily toroidally symmetric.

To study the changes in the flow and kinetic edge profiles due to MPs and possible 3D effects, we conducted dedicated experiments in which we only changed the orientation of the MP field while maintaining the same applied poloidal mode spectrum ($\Delta\varphi_{\text{UL}} \approx 135^\circ$) and the MP-field strength to its maximum $\delta B_r^{\text{res}}/B_T \approx 3 \times 10^{-4}$. Figure 8 shows time traces relative to the NBI onset from 6 L–H transitions, including four different orientations and two reference cases

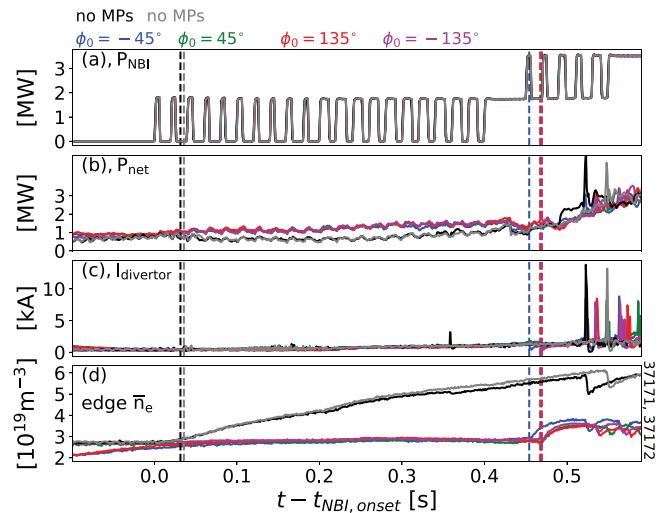


FIG. 8. Time traces relative to the NBI onset from several L–H transitions using $\Delta\varphi_{\text{UL}} = 135^\circ$ but different absolute toroidal orientations ϕ_0 (colored) to probe possible 3D effects and no MPs references (black, gray). Panels show (a) NBI power (P_{NBI}), (b) net heating power (P_{NET}), (c) divertor current, and (d) line averaged density using an edge chord. Vertical lines indicate the timing of the L–H transitions. L–H transitions with MPs are significantly delayed and do not depend on ϕ_0 .

without MPs. MPs postpone the L–H transition by more than 400 ms. All L–H transitions with MPs appear almost at the same time in the NBI ramp indicating a good reproducibility of these experiments. This is further underlined by the fact that the time-traces of P_{NET} in Fig. 8(b) and density in Fig. 8(d) from different orientations overlap.

A small caveat of these experiments is that the position control system of AUG⁴¹ moves to the outer position of the entire plasma further out by up to 1.5 cm depending on the orientation. This effect is due to pick up from stray fields from the MP coils on magnetic probes, which depends on the current of nearby coils. In one case $\phi_0 = +135^\circ$ (red in Fig. 8), R_{sep}^{axi} is around 2.16 m instead of 2.145 – 2.15 m, which slightly increases the perturbation amplitude due to the smaller distance between the MP coils and the plasma surface. An impact from an $n = 2$ intrinsic error field on these experiments is not observed, which is in line with measurements from earlier intrinsic error field studies.³⁴

A. 3D electron density and temperature profiles

First, we analyze changes in the edge electron density and temperature profiles from the orientation scan. Figure 9 shows edge profiles before the L–H transition with varying MP field orientations using $\Delta\phi_{UL} = +135^\circ$ (colored) and no MPs references (black and gray). The electron temperature (T_e) profiles with MPs are clearly elevated from 150 to 200 eV in comparison to the no MPs references, whereas within the measurement uncertainties, no change is seen in the n_e profiles. Moreover, there is no significant variation between different orientations. Only $\phi_0 = +135^\circ$ shows a slightly lower T_e , which is attributed to the larger R_{sep}^{axi} ($R_{sep}^{axi} \approx 2.16$ m) and, thus, larger

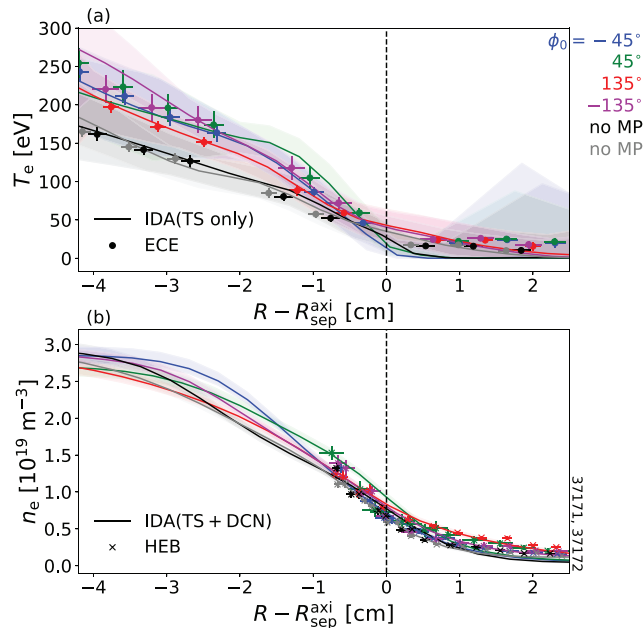


FIG. 9. Edge electron temperature (T_e) and electron density (n_e) profiles vs major radius (R) relative to R_{sep}^{axi} within a 40 ms window before the L–H transition (Fig. 8). (a) T_e profiles from ECE (circles) and IDA based on TS (solid line). (b) n_e profiles from HEB and IDA combining TS and line integrated interferometry measurements DCN. No changes in n_e are seen, whereas the T_e profiles at the L–H transition are clearly elevated with MPs because of more heating power.

MP-field strength. Our measurements suggests that 3D variations in the electron kinetic profiles are not significant, which is expected from VMEC and MARS-F calculations. Both predict a small corrugation at the outer midplane when $\Delta\phi_{UL} = +135^\circ$ is applied [see Fig. 4(c)].

B. 3D $E \times B$ velocity profiles at L–H transition

Particularly important for the physics of the L–H transition is the dynamics and structure of the $v_{E \times B}$ profiles at the edge. Previous studies at AUG suggested that the E_r profile and, thus, $v_{E \times B}$ in low-density L-modes ($n_e \approx 2.0 \times 10^{19} \text{ m}^{-3}$) vary toroidally in the presence of external MPs.²¹ In our experiments, measurements from HES indicate that this is not the case for the presented conditions with densities around $\approx 3.3 \times 10^{19} \text{ m}^{-3}$ (Fig. 10). All cases with MPs show a very similarly elevated $v_{E \times B}$ profile with respect to the no MPs case and to the critical $v_{E \times B}$ minimum from Ref. 8 (gray vertical bar in Fig. 10). Here, positive values are in the ion diamagnetic direction (IDD), whereas negative values are in the electron diamagnetic direction (EDD). Although there are small differences in the $v_{E \times B}$ minimum between the different orientations, we attribute those with slightly different MP-field strengths due to the aforementioned changes in the plasma position. For example, $\phi_0 = +135^\circ$ (red Fig. 10) has the $v_{E \times B}$ profile with the largest shift into the IDD but has also the largest R_{sep}^{axi} and, hence, MP field strength.

To unravel the changes in $v_{E \times B}$ and its different contribution, we analyze the radial force balance using the CXRS measurements from N^{7+} . To allow a comparison to DR (one sweep takes 110 ms) in the case with MPs, we adjusted the NBI power and skipped the second step of the NBI ramp (see Fig. 8) to achieve a roughly 100 ms long phase with constant heating power before a sawtooth crash induces the L–H transition. The no MPs reference from CXRS is particularly challenging to measure. Already the first or second short blip induces the L–H transition due to the low P_{LH} at low B_T . The duration of these first blips is not sufficient to acquire reasonable CXRS data. To this end,

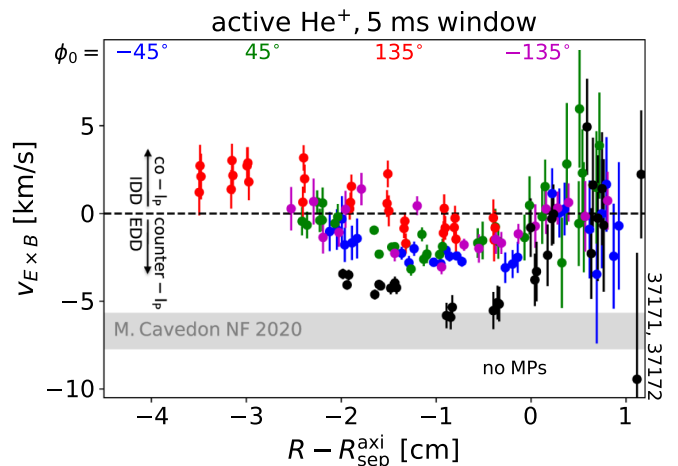


FIG. 10. $v_{E \times B}$ profiles vs R relative to R_{sep}^{axi} before the L–H transition measured by HES. Datapoints from different MP field orientations are colored, and no MPs are black. No significant 3D structure of the $v_{E \times B}$ profile is seen, and the $v_{E \times B}$ profiles with MPs are lifted compared to the no MPs case and to the critical $v_{E \times B}$ minimum from Ref. 8 (gray vertical bar).

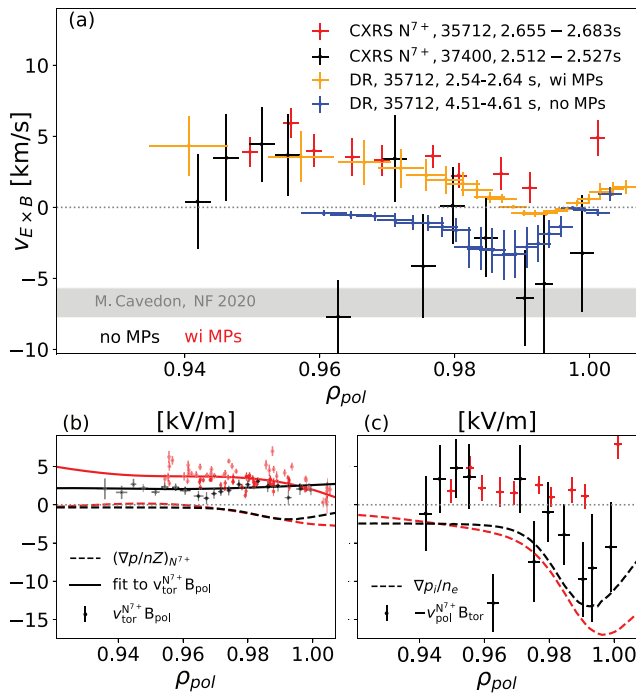


FIG. 11. (a) $v_{E \times B}$ profile vs ρ_{pol} before L–H transition with MPs using $\Delta\varphi_{UL} \approx 135^\circ$ (red circles, CXRS from N^{7+} ; orange, DR) and without MPs (black, CXRS; blue, DR) before L–H transition; (b) diamagnetic term from N^{7+} (dashed), the toroidal contribution (points), and the corresponding fit (solid); and (c) the poloidal velocity components from N^{7+} (points) in comparison to the main ion diamagnetic term (dashed). The critical $v_{E \times B}$ minimum from Ref. 8 is added as gray bar in (a).

we executed a dedicated discharge (37 400) in which we injected a 24 ms long blip to obtain acceptable CXRS data. For the no MPs reference measured by DR, we use the 100 ms long Ohmic L-mode phase before the first blip.

The results of these experiments are illustrated in Fig. 11. Panel (a) shows $v_{E \times B}$ measurements from CXRS compared to DR with MPs (black and blue) and without MPs (red and orange). Both diagnostics measure the same trend as reported previously: Without MPs, the minimum of $v_{E \times B}$ profiles is close to the -6.7 ± 1 km/s from⁸ and with MPs, it is lifted toward the co-current direction and is close to zero.

The contribution from the toroidal velocity and the diamagnetic term to E_r from N^{7+} are illustrated in Fig. 11(b). The contribution from the toroidal rotation at the L–H transition is with MPs slightly larger than the presented no MPs reference, and the associated toroidal rotation amounts roughly to 10 km/s. However, both contributions are small and we do not see such a tremendous toroidal spin-up like in DIII-D where the toroidal rotation reaches almost 25 km/s.¹⁴

A comparison between the contributions from the poloidal velocity from N^{7+} and from the main ion diamagnetic term is shown in Fig. 11(c). Since the diamagnetic term of the measured impurity is small, its poloidal velocity has to be sufficiently large to fulfill the radial force balance and is, therefore, the dominant term.³² In axisymmetric plasmas, E_r is primarily driven by the diamagnetic term from the main ions and the other terms in the radial force balance from the main ions are small. Thus, the main ion diamagnetic term is often a good

proxy for the measured E_r profile and, therefore, the measured N^{7+} poloidal velocity components [see black dashed line and black points in Fig. 11(c)]. However, this is not the case with MPs. The measured E_r and, thus, the measured N^{7+} poloidal velocity are positive, whereas the diamagnetic term of the main ions is clearly negative [see red dashed line and red points in Fig. 11(c)].

C. Radial force balance of the main ions

To investigate the difference between the measured E_r profile and the main ion diamagnetic term in the presence of MPs, we analyze the radial force balance from the main ions in more detail. Figure 12 shows E_r from N^{7+} in comparison to the main ion diamagnetic term (assuming equal ion temperatures $T_D \approx T_{N^{7+}}$ and a main ion density equal to the electron density $n_D \approx n_e$). The addition of the toroidal contribution using the toroidal velocity from N^{7+} to the main ion diamagnetic term cannot account for the difference to the measured E_r profile. This implies that either (i) the toroidal rotation of the main ions is significantly larger than the one from N^{7+} and/or (ii) the poloidal rotation of the main ions is considerably positive (ion diamagnetic direction) to fulfill the radial force balance for the main ions. Additional contributions from the Reynolds stress are not considered, because those should be reduced by MPs.⁴⁶ Figure 12(a) shows the extent of a possible main ion toroidal contribution assuming very

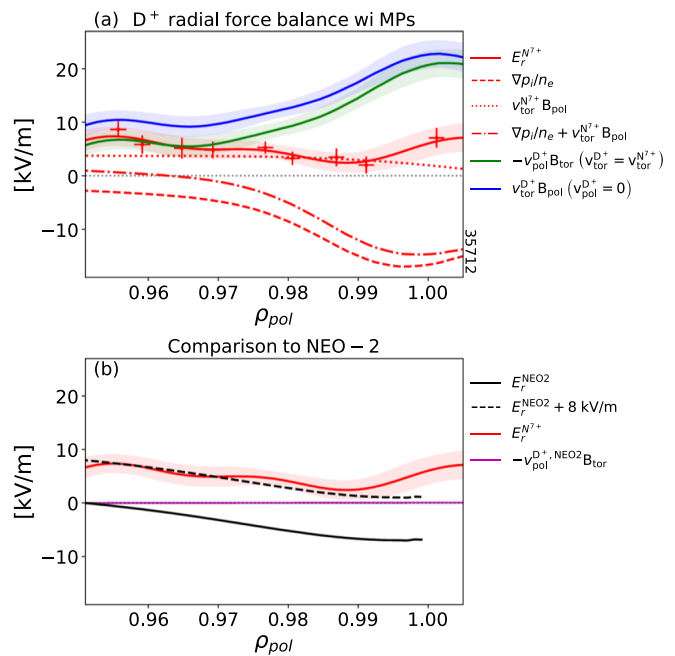


FIG. 12. Analysis of the main ion radial force balance with MPs but without main ion flow measurements. (a) Radial electric field profile from N^{7+} ($E_r^{N^{7+}}$, red solid) differs substantial from the main ion diamagnetic term (red dashed) even if the term from the toroidal rotation from N^{7+} is included (red dotted and red dashed-dotted for both terms). To fulfill the radial force balance of the main ions, the $v_{tor}^{D+} B_{pol}$ (blue) and/or $-v_{pol}^{D+} B_{tor}$ (green) terms must be considerably positive. (b) The observed positive E_r profile is not governed by 3D neoclassical theory calculated by NEO-2 (black solid), and additional 8 kV/m are needed (black dashed). Calculated $v_{pol}^{D+} B_{tor}^{NEO2}$ (magenta) is very small.

small main ion poloidal velocity $v_{\text{pol}}^{\text{D}^+} \approx 0$ m/s (blue line) and a possible main ion poloidal contribution from the main ions assuming identical toroidal velocities of D and N^{7+} , $v_{\text{tor}}^{\text{D}} \approx v_{\text{tor}}^{\text{N}^{7+}}$ (green). At the moment, flow measurements of main ions at AUG are not available to resolve whether the positive E_r is due to a positive poloidal and/or toroidal main ion flow.

Main ion flow measurements at DIII-D,⁴⁷ however, suggest that the main ion toroidal rotation can be clearly larger than the one from the impurity (carbon in this case). Although no MPs have been applied in the DIII-D experiments, these results might still be relevant for our studies since DIII-D has a considerable intrinsic $n = 1$ error field.¹⁴

The measured E_r profile is further compared to 3D neoclassical predictions from NEO-2,⁴⁸ which are based on the 3D VMEC equilibrium introduced in Sec. IV B and on kinetic profiles from 2.660 – 2.690 s from 25 712. The positive E_r profile at the edge is not captured by 3D neoclassical theory although one should note that these calculations assume $V_{\text{tor}}^{\text{D}} \approx V_{\text{tor}}^{\text{N}^{7+}}$. NEO-2 predicts a small contribution from the main ion poloidal velocity ($v_{\text{pol}}^{\text{D}^+, \text{NEO2}} B_{\text{tor}}$), and additional ≈ 8 kV/m in the co-current direction are needed to match the measured one. Interestingly, similar discrepancies between measured E_r profiles at the edge and predictions from 3D neoclassical theory have also been observed in stellarators.^{49,50}

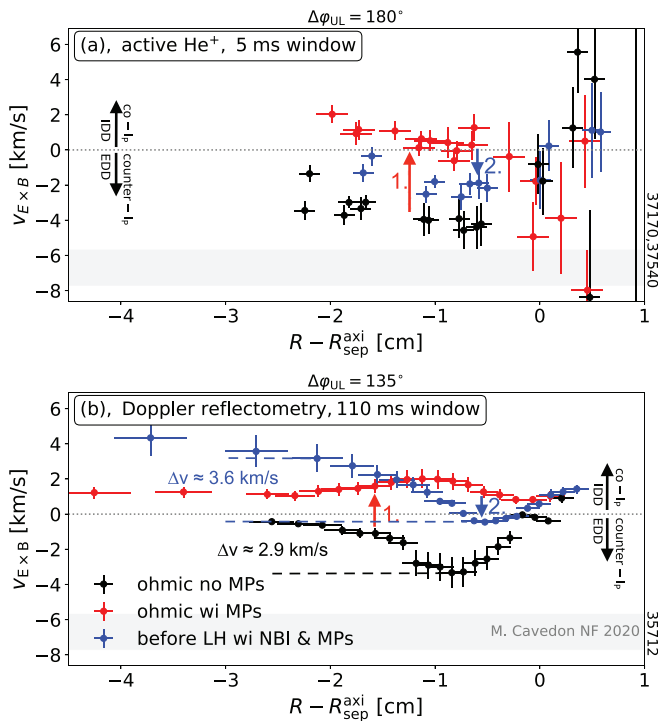


FIG. 13. $v_{E \times B}$ profile vs R using (a) HES and (b) DR during Ohmic L-mode phases without MPs (black), with MPs (red), and in the NBI heated L-mode with MPs before L–H transition (red). The gray bar shows the critical $v_{E \times B}$ minimum from Ref. 8. Both diagnostics show two important evolution steps of the $v_{E \times B}$ profile marked in the figure: (1) reversal of the $v_{E \times B}$ profile due to MPs in the Ohmic L-mode and (2) the development of the reversed E_r profile during the heating ramp. DR measurements show that the additional NBI re-establishes a shear of 3.6 km/s within 1.5 cm in the $v_{E \times B}$ profile.

D. Evolution of the $E \times B$ velocity profile

To understand the reason for the change in the $v_{E \times B}$ profile at L–H transition due to MPs, we study the preceding evolution of the $v_{E \times B}$ profile. In principle, two major steps in the development have been identified: (1) the reversal of the $v_{E \times B}$ profile due to the application of MPs during the Ohmic phase and (2) the evolution of the already reversed $v_{E \times B}$ profile throughout the NBI ramp. Both are clearly measured by DR and HES as shown in Fig. 13. Each evolution step is further analyzed in Subsections IV D 1 and IV D 2.

1. Reversal of the $E \times B$ velocity profiles due to MPs

To examine the reversal of the $v_{E \times B}$ profile, we conducted dedicated experiments in which we slowly ramped the $n = 2$ amplitude of the MP field with $\Delta\phi_{UL} \approx 135^\circ$ during an Ohmic L-mode [see Fig. 14(a)]. The density is feedback-controlled on the same density value ($n_e \approx 3.5 \times 10^{19} \text{ m}^{-3}$) as in the P_{LH} studies. Because of the enhancing particle exhaust during the ramp up, the amount of injected gas increases continuously [see Fig. 14(b)]. T_e at the edge measured by ECE and HEB almost remains constant throughout the current ramp as seen in Fig. 14(a) and later in Fig. 15(c). Particularly interesting is the dynamics of the $v_{E \times B}$ profile shown in Fig. 14(c). Throughout the MP-field ramp, the $v_{E \times B}$ profile slowly evolve until 2.72 s (t_0), then suddenly the profiles reverse. This is accompanied by a small drop in

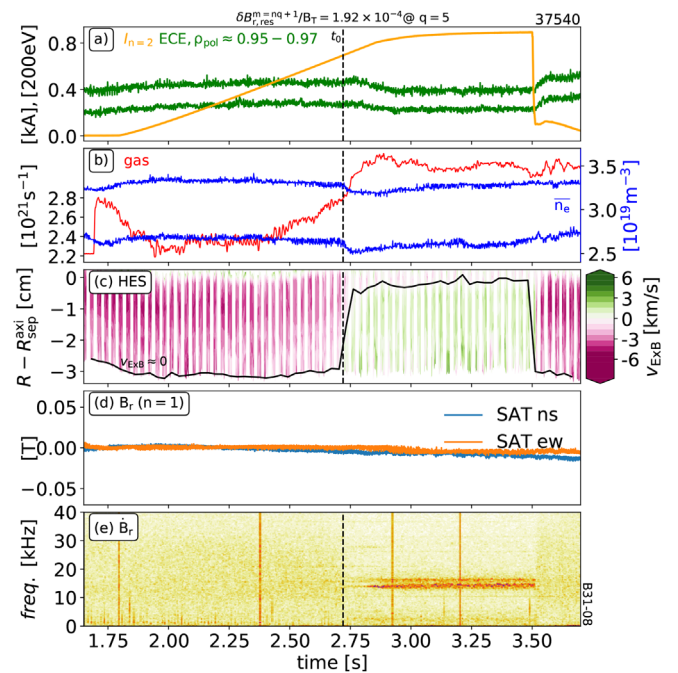


FIG. 14. Time traces from (a) slow ramp up of the $n = 2$ current amplitude applying $\Delta\phi_{UL} \approx 135^\circ$ (orange) and T_{rad} from ECE at the edge (green), (b) and line averaged density (blue) and injected gas rate (red), contour-plot of (c) $v_{E \times B}$ profiles from HES with the black line showing $v_{E \times B} \approx 0$ and (d) $n = 1$ locked mode detector with north–south (SAT ns, blue) and east–west (SAT ew, orange) orientation showing no $n = 1$ locked mode, (e) spectrogram from a pickup probe measuring the radial field perturbation at the outer midplane. The reversal takes place at $t_0 \approx 2.72$ s, when $\delta B_r^{nq+1}/B_r$ reaches $\approx 1.9 \times 10^{-4}$ at the $q = 5$ surface.

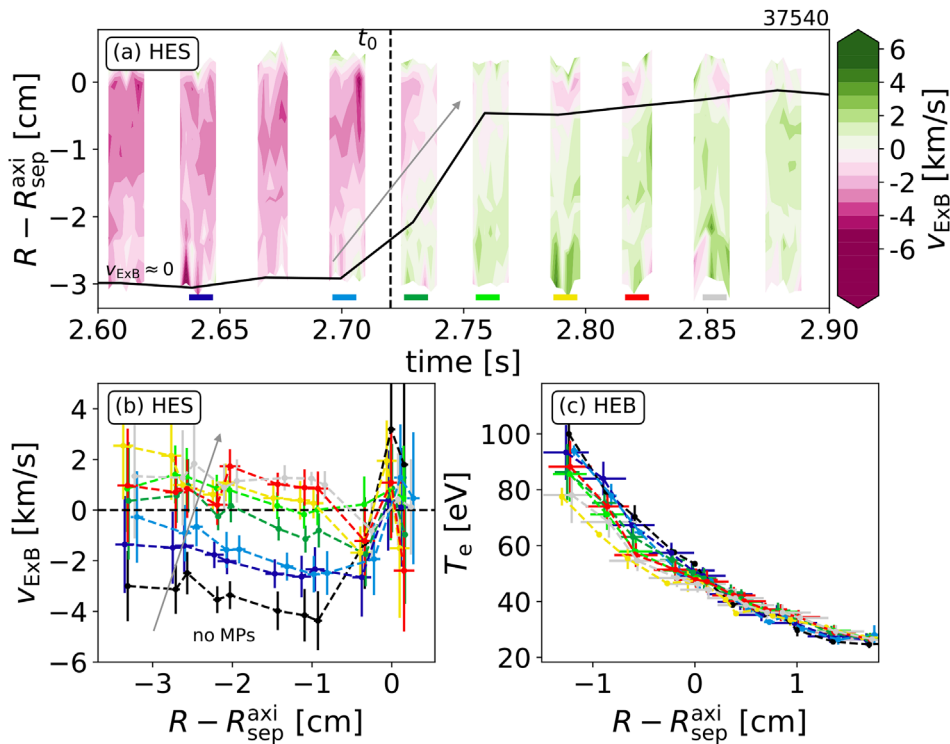


FIG. 15. Details of the $v_{E \times B}$ reversal showing the contour-plot of (a) $v_{E \times B}$ profiles from HES [zoom from Fig. 14(c)], (b) $v_{E \times B}$ profiles at certain time windows marked by colored bars in (a). (c) The corresponding T_e profiles from HEB. The $v_{E \times B}$ profile reverses inside-out (gray arrows), and T_e inside the last closed flux surface (LCFS) is dropping by ≈ 15 eV.

the line averaged edge density from 2.7 to $2.6 \times 10^{19} \text{ m}^{-3}$. After the $v_{E \times B}$ profile is fully reversed, a mode with a frequency $f = 18 \text{ kHz}$ develops as seen by the magnetic measurements. Such a mode in the presence of MPs has also been reported in Refs. 14 and 21, and DR measurements suggests that this mode is a geodesic acoustic mode (GAM).

Figure 15 shows further details of the dynamics of the $v_{E \times B}$ reversal. In the presented case, the reversal takes $50 - 70 \text{ ms}$, while slowly ramping the MP field. Furthermore, $v_{E \times B}$ at the channels further inside reverses first and then further outward showing that the $v_{E \times B}$ profile reverses inside-out [Fig. 15(b)]. T_e profiles inside the plasma boundary are only slightly affected and do not change by more than 15 eV [Fig. 15(c)]. The implication of these observations will be discussed in more detail in Sec. V. More aspects about the reversal of the E_r profile due to MPs at AUG are reported in Ref. 21.

Notably, the $v_{E \times B}$ profile reverses suddenly when the relative perturbation of the $nq + 1$ component at the edge $\delta B_r^{nq+1}/B_T$ exceeds 1.92×10^{-4} , which is in very good agreement with the critical value needed to increase P_{LH} . This is a strong indication that the reversal of the $v_{E \times B}$ profile, and the increase in P_{LH} are connected.

2. Evolution of reversed $E \times B$ velocity profiles during heating ramp

To study the evolution of the already reversed $v_{E \times B}$ profile throughout the NBI ramp, Fig. 16 shows velocity and temperature profiles from N^{7+} . The ion temperature in the core and in the edge increases, while the plasma density remains approximately the same

indicating a rise in the ion diamagnetic term of N^{7+} and of the main ions as well assuming $T_{N^{7+}} = T_D$. Because of the co-current NBI, the toroidal velocity in the core spins up, but notably this is not the case at the edge. The edge toroidal velocity of N^{7+} even reduces and, moreover, its shear develops from a positive one to a negative one around $\rho_{\text{pol}} \approx 0.97 - 0.99$. Consequently, the reversed $v_{E \times B}$ profile at the edge cannot be attributed to the increased torque from the NBI. In contrast, the edge poloidal velocity profile of N^{7+} remains the same within the measurement uncertainties. The evolution of the temperature gradient and the toroidal velocity at the edge suggest a modification of the edge $v_{E \times B}$ profile throughout the NBI ramp. This is supported by $v_{E \times B}$ profiles measured by DR (Fig. 17). Before the NBI ramp, the $v_{E \times B}$ profile is flat and reversed due to MPs. The addition of NBI leads to a formation of a well in the $v_{E \times B}$ profile and afterward in a development of a sheared profile. The evolution to a sheared $v_{E \times B}$ profile with a pronounced well is stepwise rather than gradual.

E. Alignment of MP field and $E \times B$ velocity profiles at L-H transition

So far, we have been analyzed the alignment of the MP field ($\Delta\phi_{UL} \approx 135^\circ - 180^\circ$), which has the strongest effect on the $v_{E \times B}$ profile and P_{LH} . Figure 18 shows a comparison of $v_{E \times B}$ profiles from HES for different $\Delta\phi_{UL}$ (and P_{LH}) before the L-H transition. One example has been added with an obvious $2/1$ locked mode using $\Delta\phi_{UL} \approx +95^\circ$, which results in an increased P_{LH} and even a stronger shift of the $v_{E \times B}$ profile into the IDD. This comparison shows that the

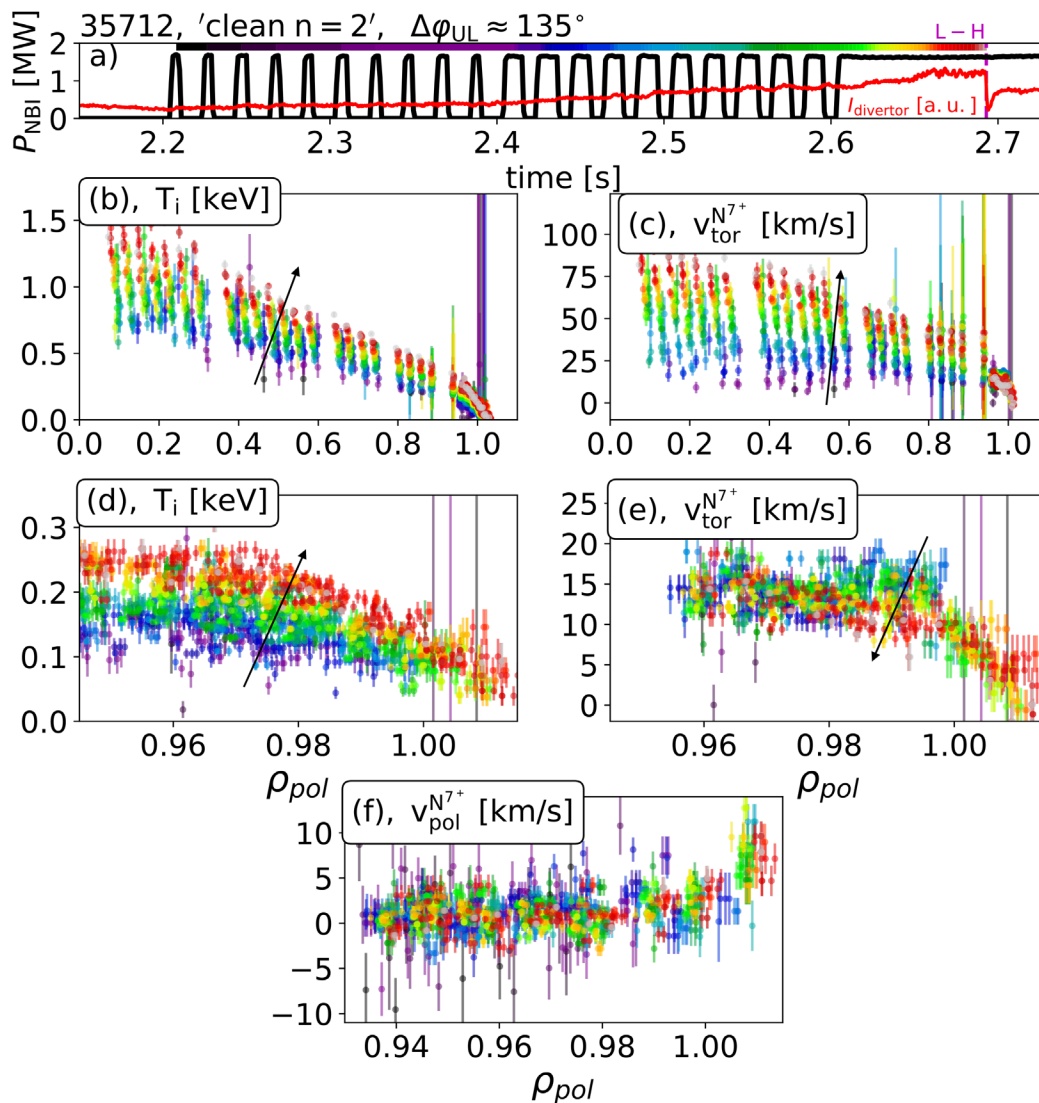


FIG. 16. Evolution of N^{7+} profiles from CXRS throughout the NBI ramp in (a). Panels show (b) core temperature, (c) core toroidal velocity, (d) edge temperature, (e) edge toroidal velocity, and (f) edge poloidal velocity. Colors in (b)–(f) indicates timing during the NBI ramp shown at the top of (a). Ion temperature and core toroidal velocity are increasing while the edge toroidal velocity even reduces indicated by black arrows. The poloidal velocity remains constant during the NBI ramp.

better the alignment of the MP field in terms of the amplitude from relevant poloidal mode components, e.g., $\delta B_r^{m+1}(\Delta\varphi_{\text{UL}} = 180^\circ) > \delta B_r^{m+1}(\Delta\varphi_{\text{UL}} = 229^\circ)$, the stronger the torque from the MPs (see Sec. V). More heating is then required to overcome the flattening in the $v_{E \times B}$ profile from the torque and to access H-mode. This results in a stronger shift of the $v_{E \times B}$ profile into the IDD, which, therefore, correlates with P_{LH} [Fig. 18(b)].

V. COMPARISON OF MODELS

In this section, we discuss possible models to explain the observed changes in the $v_{E \times B}$ profiles due to MPs with focus on the cause of the initial reversal. The following characteristics of this

reversal could be observed: (i) $v_{E \times B}$ shifts poloidally into the ion-diamagnetic direction and toroidally into the co-current direction, (ii) the reversal of the profile at the onset of the MPs propagates radially from inside the gradient region to the plasma surface, and (iii) it happens suddenly within 50 ms although the MP field is slowly increased indicating that non-linear physics causes the reversal. As discussed in Sec. IV C, the observed shift in the $v_{E \times B}$ profiles is mainly due to changes in the poloidal and/or toroidal velocity. Thus, we compare qualitatively the observed characteristics with changes in the torque due to Neoclassical Toroidal plasma Viscosity (NTV)⁵¹ from ergodization and from resonant electromagnetic (EM) torque.

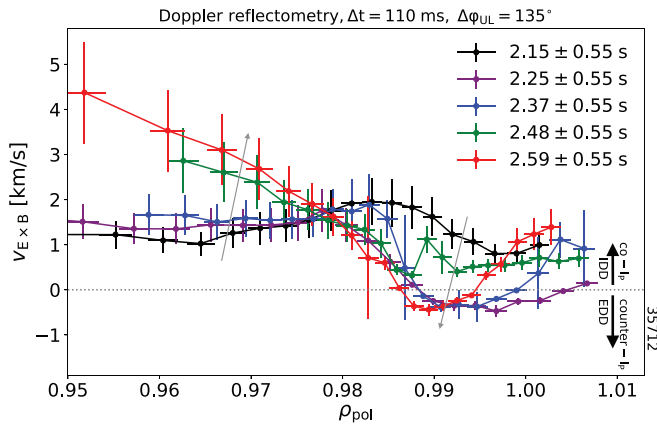


FIG. 17. Evolution of the $v_{E \times B}$ profiles from DR throughout the NBI ramp from Fig. 16. Gray arrows indicate the development of the $v_{E \times B}$ profiles. The well in $v_{E \times B}$ profile develops first and then the shear between $\rho_{pol} = 0.97$ and 0.99 .

A. Neoclassical toroidal plasma viscosity

NTV torque acts on the plasma flow due to the non-ambipolar radial flow of trapped particles induced by non-axisymmetric geometry.⁵¹ NTV drags the plasma rotation toward the neoclassical offset frequency Ω_{NC} . Depending on the initial plasma rotation relative to Ω_{NC} , NTV torque can spin up/brake the plasma into the co-current¹⁷ and countercurrent direction, which, in turn, can act into the IDD and EDD, respectively. To test, if the observed spin-up of the $v_{E \times B}$ into the co-current/IDD direction can be explained by NTV, we employed NEO-2 calculations using profile measurements as in Sec. IV C and 3D VMEC equilibrium introduced in Sec. III B before the L–H transition.

Figure 19 shows the resulting NTV torque density profile from NEO-2. According to these calculations, the NTV torque at the edge

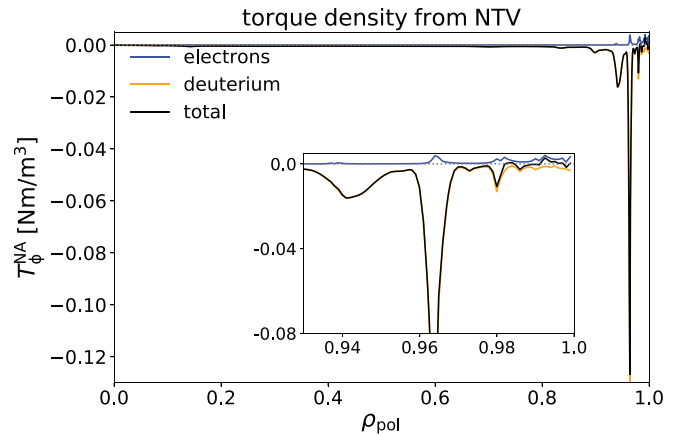


FIG. 19. Torque density profile from NEO-2 for electron and deuterium NTV based on 3D VMEC equilibrium from discharge 35712 at 2.65 s. In this case, the integrated total torque amounts to -0.036 Nm. NTV is in the countercurrent direction and is in the opposite direction than the experimental observations. The inset magnifies the edge region.

acts into the countercurrent direction and cannot explain the observed spin-up of $v_{E \times B}$ into the co-current direction.

B. Torque due to edge ergodisation

Stochastization at the edge often serves as an explanation for the reversal of the $v_{E \times B}$ and E_r profiles in the L-mode.^{10,14,52–55} In the following, we will show that plasma screening calculated by linear MHD significantly reduces the torque from stochastization inside of $\rho_{pol} < 0.98$ and cannot explain the reversal of the $v_{E \times B}$ profile in this region. The principle is based on electron losses in the stochastic field causing a parallel current along the field lines. The radial component of this current is compensated by radial ion current satisfying the ambipolarity condition $\langle j_r^e \rangle = -\langle j_r^i \rangle$. This radial ion current together with the equilibrium field exert a torque on the plasma via $\mathbf{j} \times \mathbf{B}$ torque forces. To calculate $\langle j_r^e \rangle$, we use the same recipe as described in Refs. 14 and 56, which is based on stochastic magnetic field line diffusion from the Rechester–Rosenbluth model,⁵⁷

$$j_r^e = \sigma_{ST} \left(E_r + \frac{T_e}{e n} \frac{\partial n}{\partial r} + \alpha \frac{1}{e} \frac{\partial T_e}{\partial r} \right). \quad (3)$$

σ_{ST} is the stochastic conductivity for electrons and is defined as $\sigma_{ST} = k_1 \sigma_{II} D_{ST} / L_k$ with the parallel conductivity σ_{II} , the Kolmogorov length L_k ,⁵⁸ the stochastic diffusion coefficient D_{ST} , and a numerical factor k_1 , which is the field-line loss fraction.¹⁴ α is 1.71, which corresponds to the collisional regime. In contrast to Refs. 10 and 14 D_{ST} and L_k are derived from field line tracing and the entire profile information is used [see Figs. 20(a)–20(c)]. The perturbed equilibrium for field-line tracing is generated according to Ref. 59 using the resonant radial field perturbations from MARS-F as input. Non-resonant components from the kink response are neglected, since they do not contribute to island generation and/or stochastization.⁶⁰ The following analysis is strongly influenced by the magnitude of radial field perturbations at rational surfaces, which also depends on parameters such as resistivity (η , Spitzer resistivity is used) and the fluid velocity of the electrons.

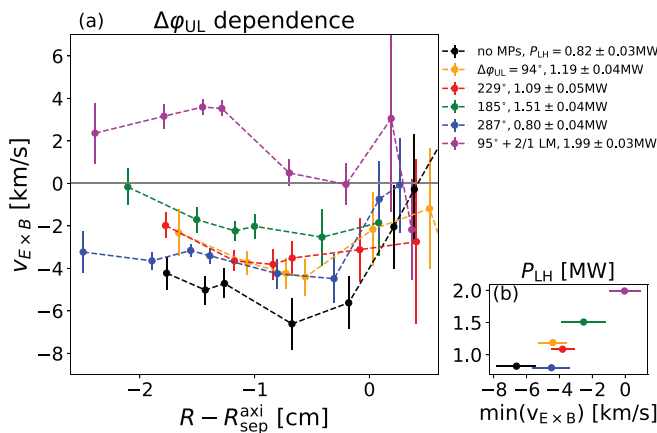


FIG. 18. (a) $v_{E \times B}$ profiles from HES before L–H transition for different $\Delta\phi_{UL}$, “no MPs” and in the presence of a clear 2/1 locked mode (LM). The legend indicates $\Delta\phi_{UL}$ and the associated P_{LH} in MW. (b) shows minimum in the $v_{E \times B}$ profiles vs associated P_{LH} . Correlation between minimum in $v_{E \times B}$ profiles and P_{LH} is seen depending on the applied poloidal mode spectrum.

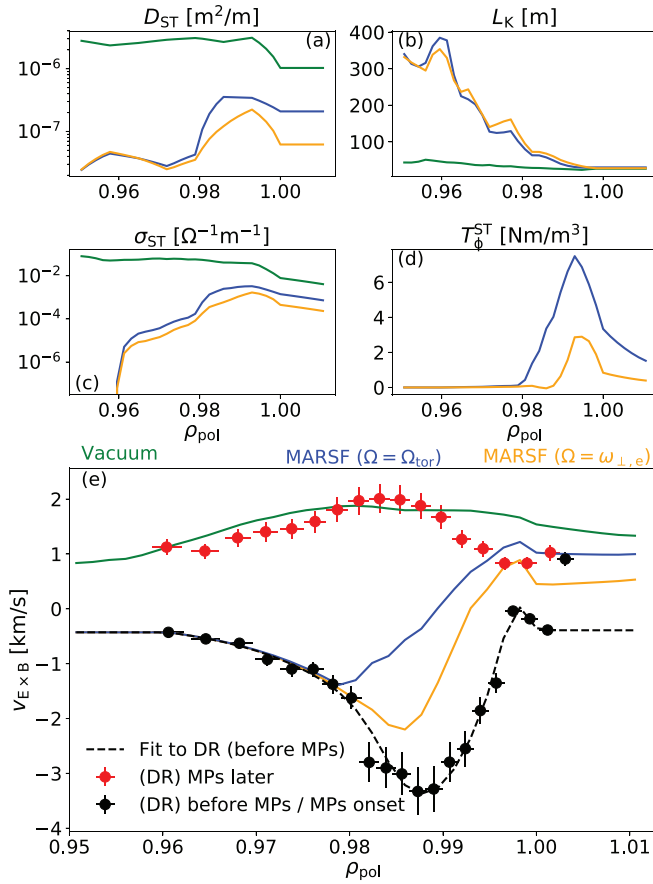


FIG. 20. Radial profiles of (a) stochastic diffusion coefficient D_{ST} , (b) the Kolmogorov length L_k , (c) stochastic conductivity σ_{ST} , (d) toroidal torque density T_ϕ^{ST} , and (e) $\mathbf{E} \times \mathbf{B}$ flow velocity $v_{E \times B}$ using the vacuum field approximation (green), MARS-F with $\Omega = \Omega_{tor}$ (blue) and with $\Omega = \omega_{\perp,e}$ (orange). Ergodisation shifts the $v_{E \times B}$ profile toward more positive values. When the linear plasma response is included, this effect is small compared to DR measurements (circles).

Since MARS-F is a single fluid MHD code, the latter one is not included. To mimic a two-fluid MHD plasma response in MARS-F, we also performed MARS-F calculations using the electron perpendicular fluid frequency ($\omega_{e,\perp} = \omega_{E \times B} + \omega_e^*$), instead of the toroidal rotation. $\omega_{e,\perp}$ are taken from the pre-MP phase with $\omega_{E \times B} = E_r / |RB_p|^{23}$ and the electron diamagnetic drift rotation defined as $\omega_e^* = p' / en$ using $p' = dp/d\psi$ with ψ in $Vs \text{ rad}^{-1}$ (see Fig. 21).

To calculate the E_r profile modified by ergodisation, the radial current due to electron loss [Eq. (3)] is set equal to the radial ion current, which is given by $\langle j_r^i \rangle = -\langle j_r^e \rangle = \sigma_{NEO}(E_r - E_r^{NEO})$ with the neoclassical conductivity $\sigma_{NEO} = (3/2)\mu_{i\perp}/R^2B^2$ using the viscosity coefficient $\mu_{i\perp} = 0.96nT_i/\nu_{ii}$. For the E_r^{NEO} profile, edge E_r measurements from DR during a phase without MPs is used. This is justified since the E_r profile without non-axisymmetric MPs are similar to the neoclassical E_r profile.^{8,61} Using Eq. (3), one can determine the modified E_r and $v_{E \times B}$ profiles.

Figure 20(e) shows the modeled $v_{E \times B}$ profile in comparison to measurements from DR. Ergodisation, as it is expected for the vacuum

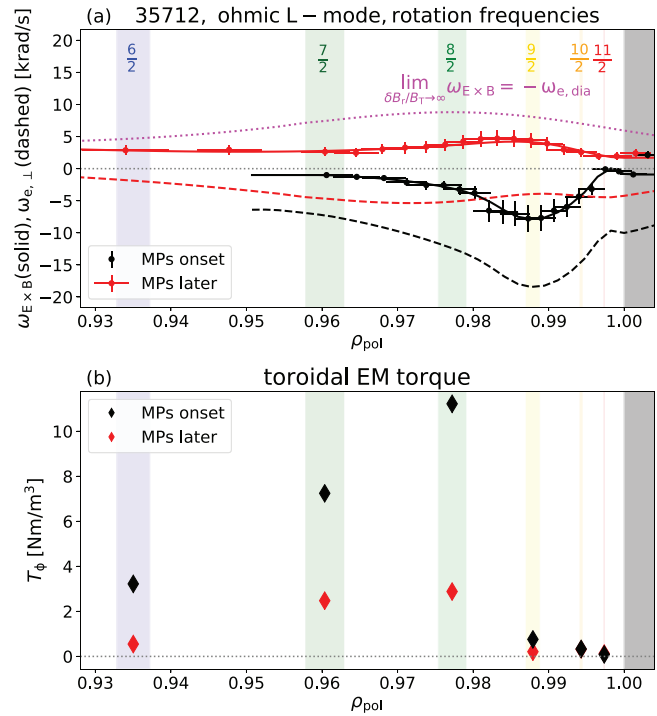


FIG. 21. (a) Radial profiles $\omega_{E \times B}$ (solid) and $\omega_{e,\perp}$ (dashed) based on DR and kinetic profile measurements at the MP onset (black) and in a later phase with MPs (red). The purple line shows $\omega_{E \times B} \approx -\omega_{e,\perp}^*$ for $\delta B_r/B \rightarrow \infty$. (b) Corresponding resonant EM torque. The plasma momentum reduces the EM torque significantly.

perturbation shown in the green curve (i.e., neglecting the plasma response) results in a positive E_r , in agreement with the experiment (red dots). Nevertheless, plasma screening decreases drastically the degree of ergodisation at the edge and the resulting changes in the E_r profile cannot explain the full reversal. Since field-line stochastization inside of $\rho_{pol} < 0.98$ is diminished, no change in E_r is seen in this region. This is mainly due to σ_{ST} , which is at least two orders of magnitude lower in this region compared to the vacuum field calculations. The toroidal torque density $T_\phi = R\langle j_r^i \rangle B_\theta$ is in the co-current direction and is situated at the very edge $\rho_{pol} = 0.98 - 1.0$ [Fig. 20(d)]. This is in contrast to previous studies¹⁴ in which the entire reversal could be explained using the quasi-linear approximation for $D_{ST} \sim |\delta B_r/B|^2$ and plasma screening calculated by M3D - C1.

The presented analysis suggests that ergodisation can spin-up the $v_{E \times B}$ profile into the IDD/co-current direction and partly explain the experimental observations. However, modeling indicates that plasma screening vastly reduces this effect such that it cannot explain the full reversal of the $v_{E \times B}$ profile, especially in the region $\rho_{pol} < 0.98$. This raises doubts whether ergodisation can explain the inside-out reversal of the $v_{E \times B}$ described in Sec. IV D 1. Moreover, according to total-f gyrokinetic calculations,⁶² Rechester-Rosenbluth is over-predicting the electron flux in the ergodic region, which implies that the changes here in E_r might also be over-predicted. Thus, another effect may also contribute to explain the full reversal.

C. Resonant electro-magnetic torque

The applications of MPs can lead to small tearing modes which are phase-locked to the external MP field.⁶³ The associated parallel current perturbation and the magnetic perturbations of the radial field exert a resonant EM torque on the plasma perpendicular to the magnetic field. According to two-fluid MHD, the plasma is then dragged toward zero $\omega_{e,\perp}$ (in the presence of static MPs). Depending on the sign and the initial $\omega_{e,\perp}$ profile, the plasma rotation can either brake or even spin-up. Figure 21(a) shows the measured $\mathbf{E} \times \mathbf{B}$ angular frequency ($\omega_{E \times B}$) and electron perpendicular fluid frequency before applying MPs (black) and in a later phase with MPs (red) in the L-mode. As shown in previous sections, the $\omega_{E \times B}$ profile reverses and the associated $\omega_{e,\perp}$ profile approaches zero during the applications of MPs. The application of MPs minimizes ($\omega_{e,\perp}$) as expected from two-fluid MHD.

To calculate the poloidal electro-magnetic torque density at the rational surfaces (r_s), we adapted the expression from⁶³

$$T_{\Theta}(r_s) = -\omega_{e,\perp} \tau_{r,s} |\delta B_{r,res}|^2 / (\mu_0 m),$$

where m is the poloidal mode number and $\tau_{r,s} = r_s^2 \mu_0 / \eta$ the resistive time scale using local plasma resistivity η , the small radius at the resonant surfaces r_s and the magnetic constant μ_0 . As in Sec. V B, $|\delta B_{r,res}|$ is deduced from MARS-F calculations using $\omega_{e,\perp}$ as the rotation input. The toroidal component of the torque density ($T_{\phi}(r_s) = n/m T_{\Theta}(r_s)$) at rational surfaces is shown in Fig. 21(b). The torque is calculated using $\omega_{e,\perp}$ before the MP application [black in Fig. 21(b)] and in a later phase with MPs (red) when the momentum is equilibrated. Figure 21 shows that the plasma reduces the EM torque to almost zero indicating that the plasma momentum equilibrates with the EM torque. Although the EM torque density at the edge is in magnitude smaller than the one from ergodisation, there is a significant EM torque density in the region $\rho_{pol} < 0.98$, which may explain the reversal of $\omega_{E \times B}$ in this region.

Our analysis suggests that the resonant EM torque may also contribute to the reversal of the $v_{E \times B}$ profile, especially, in the region $\rho_{pol} < 0.98$. However, one should keep in mind that only the linear response is taken into account. Non-linear plasma response might be important as well, which would change the contribution from $|\delta B_{r,res}|^2$. Furthermore, we would like to emphasize that fluid modeling at the edge might be limited and collisional as well as turbulent transport might influence the resulting E_r ,⁶² i.e., via changes in the turbulent Reynolds stress.⁶⁴

VI. SUMMARY AND CONCLUSION

The impact of the MP field alignment on the L–H power threshold has been investigated. In contrast to previous studies at AUG, a significant increase in P_{LH} has been observed when the MP field is aligned to maximize the plasma response to the MP field. This alignment slightly differs from the equilibrium field pitch, and is the same needed to suppress ELMs. On the one hand, the alignment of the MP field, therefore, cannot be used to optimize suppression of ELMs while avoiding the increase in P_{LH} . On the other hand, it is observed that P_{LH} increases only when the applied relative field perturbation $\delta B_r/B_T$ of the poloidal component $m = nq + 1$ exceeds $1.7 - 2 \times 10^{-4}$. This value is above one, which is required to sustain ELM suppression at AUG. This opens a window for the MP field strength in which ELM suppression is

possible without any increase in P_{LH} . Previous studies at AUG^{19,20} used an MP field strength below this critical value, which explains the absence of an increase in P_{LH} due to external MPs (other parameters such as n_e may also contribute). The observations at AUG are now in line with the results from other machines such as KSTAR^{16,17} ($n = 1$) and DIII-D^{14,15} ($n = 3$) although different toroidal mode numbers have been applied. We observe (i) a similar critical value $\delta B_r/B_T \sim 2 \times 10^{-4}$ and that (ii) P_{LH} can increase by 50% – 100%.

The increase in P_{LH} is mainly attributed to changes in the $v_{E \times B}$ profile at the edge. Dedicated experiments have shown that the $v_{E \times B}$ profile flattens and reverses from the electron diamagnetic direction/countercurrent to the ion diamagnetic direction/co-current direction. The described plasma conditions (see Sec. II) require a relative field perturbation of $\approx 1.9 \times 10^{-4}$ to observe a reversal of $v_{E \times B}$ at the edge. This is the same critical value that is needed to increase P_{LH} , which suggests that two phenomena are connected. The reversal of the $v_{E \times B}$ profile shows an inside-out evolution, i.e., $v_{E \times B}$ around $\rho_{pol} \approx 0.97$ reverses first. It occurs suddenly (within 50 – 70 ms) although the MP field has been ramped slowly, which indicates that non-linear physics is involved.

Our measurements suggest that additional heating power is needed to roughly form the same well in the $v_{E \times B}$ profile without MPs [see Fig. 13(b)]. The resulting $v_{E \times B}$ profile is shifted into the ion diamagnetic direction/co-current direction. In this case, minimum $v_{E \times B}$ is not a good approximation for the shear in the presence of MPs.⁸ One should note that our results are in agreement with previous studies at ASDEX Upgrade,⁷ because two statements are still valid: (i) The T_i profile is the main actuator to drive the ion diamagnetic term of the main ions and, thus, the shear in the $v_{E \times B}$ profile. (ii) The shear in the $v_{E \times B}$ profile plays a key role in the physics of the L–H transition. The difference in the experiments in Ref. 7 is that the torque from the MPs flattens the initial $v_{E \times B}$ profile in the L-mode and more heating power is necessary to get a similar shear without MPs.

Several models to explain the additional torque and, thus, the reversal of the $v_{E \times B}$ profile into the IDD/co-current direction of the $v_{E \times B}$ profile because of MPs are reviewed. NTV cannot explain the reversal since, according to NEO-2, it acts into the countercurrent direction. Ergodisation may partly explain the reversal but diminishes inside of $\rho_{pol} < 0.98$ due to plasma screening. Resonant EM torque in the two-fluid MHD may also explain the reversal, since the plasma minimizes the electron fluid velocity and, thus, minimizes the resonant EM torque. For the latter two scenarios, the linear plasma response from MARS-F has been used. This is likely not sufficient to model the reversal of the $v_{E \times B}$ profile and its dynamics. More quantitative modeling requires non-linear two-fluid MHD calculations with realistic resistivity and divertor geometry.

ACKNOWLEDGMENTS

This work has been carried out within the framework of the EUROfusion Consortium and has received funding from the Euratom research and training programme 2014–2018 and 2019–2020 under Grant Agreement No. 633053. The views and opinions expressed herein do not necessarily reflect those of the European Commission.

AUTHOR DECLARATIONS

Conflict of Interest

There is no conflict of interest.

DATA AVAILABILITY

The data that support the findings of this study are available from the corresponding author upon reasonable request.

REFERENCES

- ¹A. Loarte, G. Saibene, R. Sartori, D. Campbell, M. Becoulet, L. Horton, T. Eich, A. Herrmann, G. Matthews, N. Asakura, A. Chankin, A. Leonard, G. Porter, G. Federici, G. Janeschitz, M. Shimada, and M. Sugihara, *Plasma Phys. Controlled Fusion* **45**(9), 1549–1569 (2003).
- ²G. T. A. Huijsmans, C. S. Chang, N. Ferraro, L. Sugiyama, F. Waelbroeck, X. Q. Xu, A. Loarte, and S. Futatani, *Phys. Plasmas* **22**, 021805 (2015).
- ³A. W. Leonard, A. M. Howald, A. W. Hyatt, T. Shoji, T. Fujita, M. Miura, N. Suzuki, S. Tsuji, and JFT-2M Group, *Nucl. Fusion* **31**(8), 1511 (1991).
- ⁴Y. R. Martin, T. Takizuka, and ITPA CDBM H-mode Threshold Data Group, *J. Phys.* **123**(1), 012033 (2008).
- ⁵R. Groebner, K. Burrell, and R. Seraydarian, *Phys. Rev. Lett.* **64**(25), 3015 (1990).
- ⁶H. Biglari, P. H. Diamond, and P. W. Terry, *Phys. Fluids B* **2**(1), 1–4 (1990).
- ⁷F. Ryter, L. Barrera Orte, B. Kurzan, R. M. McDermott, G. Tardini, E. Viezzer, M. Bernert, R. Fischer, and ASDEX Upgrade Team, *Nucl. Fusion* **54**(8), 083003 (2014).
- ⁸M. Cavedon, G. Birkenmeier, T. Pütterich, F. Ryter, E. Viezzer, E. Wolftrum, R. Dux, T. Happel, P. Hennequin, U. Plank, U. Stroth, M. Willensdorfer, and ASDEX Upgrade Team, *Nucl. Fusion* **60**(6), 066026 (2020).
- ⁹P. Sauter, T. Pütterich, F. Ryter, E. Viezzer, E. Wolftrum, G. D. Conway, R. Fischer, B. Kurzan, R. M. McDermott, S. K. Rathgeber, and ASDEX Upgrade Team, *Nucl. Fusion* **52**(1), 012001 (2011).
- ¹⁰V. Rozhansky, P. Molchanov, E. Kaveeva, S. Voskoboynikov, A. Kirk, E. Nardon, D. Coster, and M. Tendler, *Nucl. Fusion* **51**(8), 083009 (2011).
- ¹¹A. Kirk, Y. Liu, E. Nardon, P. Tamain, P. Cahyna, I. Chapman, P. Denner, H. Meyer, S. Mordijck, D. Temple, and MAST Team, *Plasma Phys. Controlled Fusion* **53**(6), 065011 (2011).
- ¹²R. Scannell, A. Kirk, M. Carr, J. Hawke, S. S. Henderson, T. O’Gorman, A. Patel, A. Shaw, A. Thornton, and MAST Team, *Plasma Phys. Controlled Fusion* **57**(7), 075013 (2015).
- ¹³S. Mordijck, T. L. Rhodes, L. Zeng, E. J. Doyle, L. Schmitz, C. Chrystal, T. J. Strait, and R. A. Moyer, *Plasma Phys. Controlled Fusion* **58**(1), 014003 (2015).
- ¹⁴L. Schmitz, D. M. Kriete, R. S. Wilcox, T. L. Rhodes, L. Zeng, Z. Yan, G. R. McKee, T. E. Evans, C. Paz-Soldan, P. Gohil, B. Lyons, C. C. Petty, D. Orlov, and A. Marinoni, *Nucl. Fusion* **59**(12), 126010 (2019).
- ¹⁵P. Gohil, T. E. Evans, M. E. Fenstermacher, J. R. Ferron, T. H. Osborne, J. M. Park, O. Schmitz, J. T. Scoville, and E. A. Unterberg, *Nucl. Fusion* **51**(10), 103020 (2011).
- ¹⁶Y. In, J.-K. Park, Y. M. Jeon, J. Kim, G. Y. Park, J.-W. Ahn, A. Loarte, W. H. Ko, H. H. Lee, J. W. Yoo, J. W. Juhn, S. W. Yoon, and H. Park, *Nucl. Fusion* **57**(11), 116054 (2017).
- ¹⁷H. K. Park, M. J. Choi, S. H. Hong, Y. In, Y. M. Jeon, J. S. Ko, W. H. Ko, J. G. Kwak, J. M. Kwon, J. Lee *et al.*, *Nucl. Fusion* **59**(11), 112020 (2019).
- ¹⁸S. M. Kaye, R. Maingi, D. Battaglia, R. E. Bell, C. S. Chang, J. Hosea, H. Kugel, B. P. LeBlanc, H. Meyer, G. Y. Park, and J. R. Wilson, *Nucl. Fusion* **51**(11), 113019 (2011).
- ¹⁹F. Ryter, S. K. Rathgeber, E. Viezzer, W. Suttrop, A. Burckhart, R. Fischer, B. Kurzan, S. Potzel, T. Pütterich, and ASDEX Upgrade Team, *Nucl. Fusion* **52**(11), 114014 (2012).
- ²⁰F. Ryter, S. K. Rathgeber, L. Barrera Orte, M. Bernert, G. D. Conway, R. Fischer, T. Happel, B. Kurzan, R. M. McDermott, A. Scarabosio, W. Suttrop, E. Viezzer, M. Willensdorfer, E. Wolftrum, and ASDEX Upgrade Team, *Nucl. Fusion* **53**(11), 113003 (2013).
- ²¹G. D. Conway, S. Fietz, H. W. Müller, T. Lunt, P. Simon, W. Suttrop, M. Maraschek, T. Happel, E. Viezzer, and ASDEX Upgrade Team, *Plasma Phys. Controlled Fusion* **57**(1), 014035 (2015).
- ²²C. Paz-Soldan, N. C. Logan, M. J. Lanctot, J. M. Hanson, J. D. King, R. J. La Haye, R. Nazikian, J.-K. Park, and E. J. Strait, *Phys. Rev. Lett.* **114**, 105001 (2015).
- ²³W. Suttrop, A. Kirk, V. Bobkov, M. Cavedon, M. Dunne, R. M. McDermott, H. Meyer, R. Nazikian, C. Paz-Soldan, D. A. Ryan, E. Viezzer, M. Willensdorfer, and ASDEX Upgrade Team, *Nucl. Fusion* **58**(9), 096031 (2018).
- ²⁴M. Teschke, N. Arden, H. Eixenberger, M. Rott, and W. Suttrop, *Fusion Eng. Des.* **96**, 171–176 (2015).
- ²⁵W. Suttrop, D. Hahn, J. Hartmann, A. Herrmann, M. Rott, B. Streibl, W. Treutterer, T. Vierle, D. Yadikin, I. Zammuto, E. Gaio, V. Toigo, P. Brunzell, E. Olofsson, and ASDEX Upgrade Team, “Physical description of external circuitry for resistive wall mode control in ASDEX Upgrade,” in *36th EPS Conference on Plasma Physics, Sofia* (ECA, 2009), Vol. 33E, pp. 1–4.
- ²⁶M. Willensdorfer, S. S. Denk, E. Strumberger, W. Suttrop, B. Vanovac, D. Brida, M. Cavedon, I. Classen, M. Dunne, S. Fietz, R. Fischer, A. Kirk, F. M. Laggner, Y. Q. Liu, T. Odstrčil, D. A. Ryan, E. Viezzer, H. Zohm, I. C. Luhmann, and ASDEX Upgrade Team, *Plasma Phys. Controlled Fusion* **58**(11), 114004 (2016).
- ²⁷S. S. Denk, R. Fischer, H. M. Smith, P. Helander, O. Maj, E. Poli, J. Stober, U. Stroth, W. Suttrop, E. Westerhof, M. Willensdorfer, and ASDEX Upgrade Team, *Plasma Phys. Controlled Fusion* **60**(10), 105010 (2018).
- ²⁸M. Griener, J. M. M. Burgos, M. Cavedon, G. Birkenmeier, R. Dux, B. Kurzan, O. Schmitz, B. Sieglin, U. Stroth, E. Viezzer, E. Wolftrum, and ASDEX Upgrade Team, *Plasma Phys. Controlled Fusion* **60**(2), 025008 (2017).
- ²⁹R. Fischer, C. J. Fuchs, B. Kurzan, W. Suttrop, E. Wolftrum, and ASDEX Upgrade Team, *Fusion Sci. Technol.* **58**, 675–682 (2010).
- ³⁰A. Mlynek, M. Reich, L. Giannone, W. Treutterer, K. Behler, H. Blank, A. Buhler, R. Cole, H. Eixenberger, R. Fischer, A. Lohs, K. Lüddecke, R. Merkel, G. Neu, F. Ryter, D. Zasche, and ASDEX Upgrade Team, *Nucl. Fusion* **51**, 043002 (2011).
- ³¹E. Viezzer, T. Pütterich, R. Dux, R. M. McDermott, and ASDEX Upgrade Team, *Rev. Sci. Instrum.* **83**(10), 103501 (2012).
- ³²M. Cavedon, T. Pütterich, E. Viezzer, R. Dux, B. Geiger, R. M. McDermott, H. Meyer, U. Stroth, and ASDEX Upgrade Team, *Rev. Sci. Instrum.* **88**(4), 043103 (2017).
- ³³U. Plank *et al.*, “Development of a HeII spectroscopy diagnostic at ASDEX Upgrade to measure the Er gradient across the separatrix,” (unpublished 2022).
- ³⁴M. Maraschek, S. Fietz, A. Gude, S. Günter, R. Koslowski, K. Lackner, K. Lüders, T. Lunt, G. Pautasso, E. Strumberger, W. Suttrop, Q. Yu, H. Zohm, and ASDEX Upgrade Team, “Measurement and impact of the $n = 1$ intrinsic error field at ASDEX Upgrade,” in *40th Conference EPS Plasma Physics, 1–5 July 2013* (European Physical Society, 2014).
- ³⁵C. F. Maggi, H. Weisen, J. C. Hillesheim, A. Chankin, E. Delabie, L. Horváth, F. Auriemma, I. S. Carvalho, G. Corrigan, J. Flanagan, L. Garzotti, D. Keeling, D. King, E. Lerche, R. Lorenzini, M. Maslov, S. Menuir, S. Saarelma, A. C. C. Sips, E. R. Solano, E. Belonohy, F. J. Casson, C. Challis, C. Giroud, V. Parail, C. Silva, M. Valisa, and JET Contributors, *Plasma Phys. Controlled Fusion* **60**(1), 014045 (2018).
- ³⁶L. M. Shao, E. Wolftrum, F. Ryter, G. Birkenmeier, F. M. Laggner, E. Viezzer, R. Fischer, M. Willensdorfer, B. Kurzan, T. Lunt, and ASDEX Upgrade Team, *Plasma Phys. Controlled Fusion* **58**(2), 025004 (2016).
- ³⁷D. A. Ryan, Y. Q. Liu, A. Kirk, W. Suttrop, B. Dudson, M. Dunne, R. Fischer, J. C. Fuchs, M. Garcia-Munoz, B. Kurzan, P. Piovesan, M. Reinke, M. Willensdorfer, and ASDEX Upgrade Team, *Plasma Phys. Controlled Fusion* **57**(9), 095008 (2015).
- ³⁸Y. Liu, D. Ryan, A. Kirk, L. Li, W. Suttrop, M. Dunne, R. Fischer, J. C. Fuchs, B. Kurzan, P. Piovesan, M. Willensdorfer, and ASDEX Upgrade Team, *Nucl. Fusion* **56**(5), 056015 (2016).
- ³⁹C. Paz-Soldan, N. C. Logan, S. R. Haskey, R. Nazikian, E. J. Strait, X. Chen, N. M. Ferraro, J. D. King, B. C. Lyons, and J.-K. Park, *Nucl. Fusion* **56**(5), 056001 (2016).
- ⁴⁰W. Suttrop, A. Kirk, R. Nazikian, N. Leuthold, E. Strumberger, M. Willensdorfer, M. Cavedon, M. Dunne, R. Fischer, S. Fietz *et al.*, *Plasma Phys. Controlled Fusion* **59**(1), 014049 (2017).
- ⁴¹M. Willensdorfer, E. Strumberger, W. Suttrop, M. Dunne, R. Fischer, G. Birkenmeier, D. Brida, M. Cavedon, S. S. Denk, V. Igochine, L. Giannone, A.

- Kirk, J. Kirschner, A. Medvedeva, T. Odstrčil, and D. A. Ryan, *Nucl. Fusion* **57**(11), 116047 (2017).
- ⁴²N. M. Ferraro, *Phys. Plasmas* **19**(5), 056105 (2012).
- ⁴³Y. Q. Liu, J. M. Hanson, B. D. Blackwell, S. R. Haskey, M. J. Lanctot, and R. Nazikian, *Plasma Phys. Controlled Fusion* **56**(3), 035005 (2014).
- ⁴⁴P. J. McCarthy and ASDEX Upgrade Team, *Plasma Phys. Controlled Fusion* **54**, 015010 (2011).
- ⁴⁵Y. In, Y. M. Jeon, J.-K. Park, A. Loarte, J.-W. Ahn, J. H. Lee, H. H. Lee, G. Y. Park, K. Kim, H. S. Kim, W. H. Ko, T. Rhee, J. Kim, S. W. Yoon, and H. Park, *Nucl. Fusion* **59**(5), 056009 (2019).
- ⁴⁶D. M. Kriete, G. R. McKee, L. Schmitz, D. R. Smith, Z. Yan, L. A. Morton, and R. J. Fonck, *Phys. Plasma* **27**(6), 062507 (2020).
- ⁴⁷S. R. Haskey, B. A. Grierson, C. Chrystal, A. Ashourvan, K. H. Burrell, R. Groebner, E. A. Belli, L. Stagner, D. J. Battaglia, T. Stoltzfus-Dueck, and A. Bortolon, *Plasma Phys. Controlled Fusion* **60**(10), 105001 (2018).
- ⁴⁸A. F. Martitsch, S. V. Kasilov, W. Kernbichler, G. Kapper, C. G. Albert, M. F. Heyn, H. M. Smith, E. Strumberger, S. Fietz, W. Suttrop, M. Landreman, ASDEX Upgrade Team, and EUROfusion MST1 Team, *Plasma Phys. Controlled Fusion* **58**(7), 074007 (2016).
- ⁴⁹K. Ida, M. Yoshinuma, M. Yokoyama, S. Inagaki, N. Tamura, B. J. Peterson, T. Morisaki, S. Masuzaki, A. Komori, Y. Nagayama, K. Tanaka, K. Narihara, K. Y. Watanabe, C. D. Beidler, and LHD Experimental Group, *Nucl. Fusion* **45**(5), 391–398 (2005).
- ⁵⁰A. Dinklage, M. Yokoyama, K. Tanaka, J. L. Velasco, D. López-Bruna, C. D. Beidler, S. Satake, E. Ascasibar, J. Arévalo, J. Balduhn, Y. Feng, D. Gates, J. Geiger, K. Ida, M. Isaev, M. Jakubowski, A. López-Fraguas, H. Maaßberg, J. Miyazawa, T. Morisaki, S. Murakami, N. Pablant, S. Kobayashi, R. Seki, C. Suzuki, Y. Suzuki, Y. Turkin, A. Wakasa, R. Wolf, H. Yamada, and M. Yoshinuma, *Nucl. Fusion* **53**(6), 063022 (2013).
- ⁵¹K. C. Shaing, K. Ida, and S. A. Sabbagh, *Nucl. Fusion* **55**(12), 125001 (2015).
- ⁵²B. Unterberg, C. Busch, M. de Bock, J. W. Coenen, K. H. Finken, S. Jachmich, M. W. Jakubowski, Y. Kikuchi, A. Krämer-Flecken, M. Lehnen, U. Samm, O. Schmitz, S. Soldatov, M. Z. Tokar, M. von Hellermann, R. C. Wolf, and Y. Xu, *J. Nucl. Mater.* **363–365**, 698–702 (2007).
- ⁵³E. Kaveeva, V. Rozhansky, and M. Tendler, *Nucl. Fusion* **48**(7), 075003 (2008).
- ⁵⁴J. W. Coenen, O. Schmitz, B. Unterberg, M. Clever, M. A. Jakubowski, U. Samm, B. Schweer, H. Stoschus, and M. Tokar, *Nucl. Fusion* **51**(6), 063030 (2011).
- ⁵⁵S. Mordijck, R. A. Moyer, N. M. Ferraro, M. R. Wade, and T. H. Osborne, *Nucl. Fusion* **54**(8), 082003 (2014).
- ⁵⁶V. Rozhansky, E. Kaveeva, P. Molchanov, I. Veselova, S. Voskoboinikov, D. Coster, A. Kirk, S. Lisgo, and E. Nardon, “Modification of the edge transport barrier by resonant magnetic perturbations,” *Nucl. Fusion* **50**(3), 034005 (2010).
- ⁵⁷A. B. Rechester and M. N. Rosenbluth, *Phys. Rev. Lett.* **40**, 38–41 (1978).
- ⁵⁸I. Kaganovich and V. Rozhansky, *Phys. Plasma* **5**(11), 3901–3909 (1998).
- ⁵⁹D. Brida, T. Lunt, M. Wischmeier, G. Birkenmeier, P. Cahyna, D. Carralero, M. Faitsch, Y. Feng, B. Kurzan, M. Schubert, B. Sieglin, W. Suttrop, and E. Wolfrum, *Nucl. Mater. Energy* **12**, 831–837 (2017).
- ⁶⁰D. Brida, T. Lunt, M. Faitsch, M. Wischmeier, Y. Feng, W. Suttrop, U. Stroth, and T. Eich, *Nucl. Mater. Energy* **19**, 205–210 (2019).
- ⁶¹M. Cavedon, T. Pütterich, E. Viezzer, G. Birkenmeier, T. Happel, F. M. Laggner, P. Manz, F. Ryter, U. Stroth, and ASDEX Upgrade Team, *Nucl. Fusion* **57**(1), 014002 (2017).
- ⁶²R. Hager, C. S. Chang, N. M. Ferraro, and R. Nazikian, *Nucl. Fusion* **59**(12), 126009 (2019).
- ⁶³Q. Yu, S. Günter, and K. H. Finken, *Phys. Plasmas* **16**(4), 042301 (2009).
- ⁶⁴P. H. Diamond and Y.-B. Kim, *Phys. Fluids B* **3**(7), 1626–1633 (1991).